FINITE ELEMENT ANALYSIS OF GRAFT STRESS IN VARIOUS TUNNEL POSITIONS FOR ACL RECONSTRUCTION

by

Scott James Kramer

B.S. Engineering Science and Mechanics, Virginia Polytechnic and State University, 2008

Submitted to the Graduate Faculty of

Swanson School of Engineering in partial fulfillment

of the requirements for the degree of

Master of Science in Mechanical Engineering

University of Pittsburgh

2011

UNIVERSITY OF PITTSBURGH

SWANSON SCHOOL OF ENGINEERING

This thesis was presented

by

Scott James Kramer

It was defended on

November 11, 2011

and approved by

Dr. Patrick J. Smolinski, Ph.D., Associate Professor, Department of Mechanical Engineering and Materials Science

Dr. William S. Slaughter, Ph.D., Associate Professor, Department of Mechanical Engineering and Materials Science

Dr. Mark C. Miller, Ph.D., Associate Research Professor, Department of Mechanical Engineering and Materials Science

Thesis Advisor: Dr. Patrick J. Smolinski, Ph.D.

Copyright © by Scott James Kramer

2011

FINITE ELEMENT ANALYSIS OF GRAFT STRESS IN VARIOUS TUNNEL POSTIONS FOR ACL RECONSTRUCTION

Scott James Kramer, M.S.

University of Pittsburgh, 2011

The anterior cruciate ligament (ACL) is one of the most important ligaments in stabilizing the knee and injury of the ACL is one of the most common athletic injuries. The ACL has limited ability to heal due to its avascular environment; therefore, the primary treatment is to replace the ACL with a tissue graft. There is debate among clinicians on appropriate reconstruction techniques, such as the position and orientation of the graft. Improper graft placement may result in elevated forces and stresses which could lead to graft failure. This study examines the forces and stresses present in grafts when placed in five common tunnel positions, four anatomic and one non-anatomic. This was accomplished using computational models and experimental testing. Through the use of the finite element (FE) method a computational model was developed. Three-dimensional solid models of the tibia and femur were obtained through medical imaging in order to obtain the actual geometry of the bones and precise location of tunnel positions. An isotropic hyperelastic material was used to model the cylindrical grafts, placed in their respective positions. Three-dimensional joint kinematics were obtained via a six degree-of-freedom robotic manipulator and were used for input into the computational model. Graft stress and tension were calculated after the kinematics were applied for two initial conditions: stress-free and pre-stress that resulted from a 40N initial tension. Graft tension for each case was compared to experimentally determined graft force, obtained from a separate study of 16 cadaveric knee specimens. Results suggest that the FE estimation of graft tension in the 40 N tension initial condition more closely resembled experimental data and the non-anatomic graft placement resulted in elevated graft tension and stress.

TABLE OF CONTENTS

LIST OF FIGURES

1.0 INTRODUCTION

1.1 MOTIVATION

The anterior cruciate ligament (ACL) is one of the most important structures for providing stability to the knee (Zhang 2008). Its primary role is to resist anterior translation of the tibia, with a secondary role of providing rotational stability. Damage to the ACL is a common athletic injury and is one of the most widely treated conditions of the knee, with an estimated 60,000 to 175,000 cases treated each year in the United States (Lymon 2009). The ACL has limited ability to heal due to its relatively avascular environment (Danto 1993). Therefore, ACL reconstructions replace the damaged ligament with a tissue graft; either an autograft, tissue harvested from the patient, or an allograft, tissue harvested from cadavers. There is debate among clinicians on the most appropriate reconstruction technique. This includes graft position and orientation, graft selection, graft fixation. Different reconstruction techniques have resulted in varying failure rates. Failure of a graft is generally defined as an increase in laxity beyond an acceptable level. Elevated forces and stress in the graft can cause partial or full rupture, or permanent deformation which leads to increased laxity of the knee. The failure rate of ACL reconstruction as a whole is unknown, as the clinical definition of failure is vague. However, one study performed a two to five year follow-up of 63 patients who underwent primary single bundle ACL reconstruction and reported a rate of failure of 15.6 % (Snow 2010). Also, in many cases the ACL itself does not fail, but the injured knee has been shown to have a higher instance of osteoarthritis compared to the uninjured knee. One recent study found that 39% of patients who underwent ACL reconstruction 8 years prior had osteoarthritis in the injured knee, but not in the uninjured knee (Li 2011). Therefore, because of possible graft failure, abnormal knee motion and developing osteoarthritis, it is important to investigate the biomechanics and kinematics associated with various reconstruction techniques.

1.2 OBJECTIVES

The primary objective of this study is to create a finite element model of ACL grafts in various tunnel positions used in ACL reconstruction to compare the force and stress in each graft. A secondary objective is to determine the effect that a 40N initial tension has on graft behavior, compared to a zero initial tension. The results from this model will be compared to results found from experiment for a measure of validation. The outcome will provide insight into how each graft behaves under various kinematic conditions, which will benefit the clinical community by identifying graft positions that result in high stress.

2.0 BACKGROUND

Skeletal ligaments are short bands of fibrous connective tissue that bind bones together across joints. It is thought that the ACL is composed of two functional bundles of ligament, the anteriomedial bundle (AM) and the posteriolateral bundle (PL) (Wu 2009), which can be seen in Figure 1.

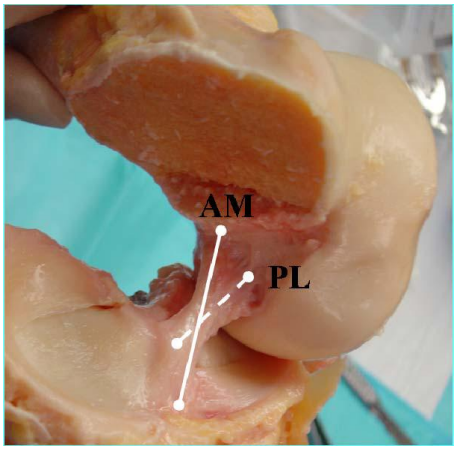

Figure 1: Bundles of the ACL: Anteriomedial (AM) and Posteriolateral (PL)

Their mechanical function is to guide normal joint motion and restrict abnormal joint motion. Ligaments can be subjected to extreme stress while performing their role in restricting abnormal movement and can be damaged when overloaded. In addition to ligament damage, abnormal joint motion of the knee may have the potential to damage articular cartilage and contribute to the progression of osteoarthritis; therefore a goal of ACL reconstruction is to restore normal joint motion. (Dayal 2005)

2.1 ACL RECONSTRUCTION

In general, there are two types of ACL reconstruction: single bundle reconstruction (SB), where the deficient ACL is replaced by a single graft and double bundle (DB) ACL reconstruction, where the ACL is replaced by two grafts. Until recently, SB reconstruction was the primary method used. Biomechanical studies have shown that SB reconstruction can effectively restore the anterior laxity associated with a deficient ACL, but is ineffective in restoring rotational laxity associated with a combined rotary load of internal and valgus torque. (Chhabra 2006). Double bundle (DB) ACL reconstruction replaces the two functional bundles of the ACL with two grafts. It is believed that the addition of a second graft mimics the more posterior and lateral PL bundle of the native ACL, thereby increasing rotational stability (Wu 2009). Figure 2 shows a DB ACL reconstruction.

Figure 2: Double Bundle ACL Reconstruction

2.1.1 Anatomic Single Bundle ACL Reconstruction

The term anatomical reconstruction refers to a technique in which the graft position matches that of the native ACL. To accomplish this, the tibial and femoral tunnels for insertion of the tissue graft, are drilled to match the native ACL's insertion sites. Since the area of a single graft with a circular tunnel usually does not cover the entire insertion site, the graft can be placed in different locations within the native insertion site. Thus, three different bone tunnel positions can be considered anatomic based on the previous definition. One places the tunnel so that the graft extends from the footprint of the AM bundle on the tibia to the footprint of the AM bundle on the femur (AM-AM). Another site connects the tibial PL bundle footprint with the femoral PL footprint (PL-PL). Lastly a graft can be positioned between the geometric centroid of the total ACL tibial and femoral footprints (MID-MID) (Kato 2010). Figure 3 shows a schematic of the three anatomic SB techniques.

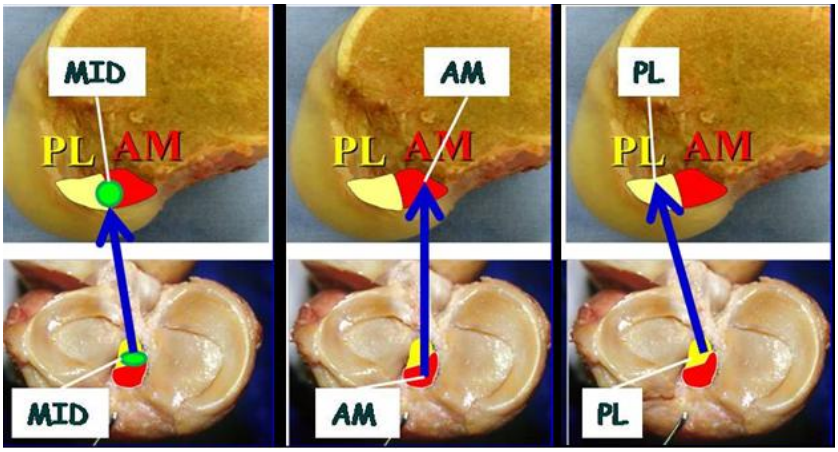

Figure 3: Schematic of three anatomic SB ACL reconstructions

2.1.2 Non-Anatomic Single Bundle ACL Reconstruction

A non-anatomical technique is defined as a tunnel placement that is outside the native ACL insertion site. A common non-anatomical reconstruction is a vertically placed femoral bone tunnel above the native femoral footprint (Figure 4).

Figure 4: A vertically oriented femoral tunnel

This non-anatomical tunnel placement often occurs from the trans-tibial surgical technique, in which the tibial and femoral tunnels are both drilled with a single drilling procedure (Kato 2010). This technique often results in a graft that is placed between the tibial PL bundle footprint and a femoral location that is high in the femoral intercondylar notch (PL-High AM), which can be seen in Figure 5 (Kato 2010). For decades, the trans-tibial technique has been the standard in SB ACL reconstruction and the non-anatomical tunnel placement associated with this technique has been suggested as a cause of clinical failure following ACL reconstruction (Bedi 2009).

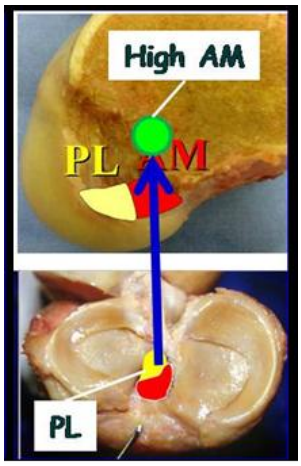

Figure 5: Schematic of the PL-High AM tunnel position

2.1.3 Anatomic Double Bundle

The anatomic DB technique combines the two anatomic single bundle techniques mentioned previously, the AM-AM technique and the PL-PL technique. Non-anatomic DB ACL reconstruction can be defined as anything other than the PL-PL/AM-AM anatomic technique. A picture of the tunnel positions can be seen in Figure 6.

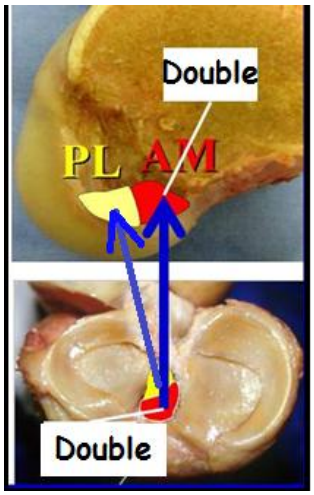

Figure 6: Tunnel placement for anatomic DB ACL reconstruction

.

2.2 FINITE ELEMENT MODELING OF LIGAMENTS

Excessive stretching or failure of ligaments can result in gross joint instability. Because these instabilities can greatly restrict the activity level of an individual, research efforts have examined ligament injury mechanism, techniques for ligament reconstruction, and rehabilitation methods for use during healing. However, fundamental mechanical questions regarding the role of individual ligaments and the efficacy of reconstructive procedures still exist. This is likely due to limitations of experimental studies such as their high cost, low sensitivity and difficulties associated with accurate measurement of mechanical parameters. The use of computational methods for the study of joint mechanics can elucidate ligament function and yield information that is difficult or impossible to obtain experimentally. In particular, the finite element (FE) method offers the ability to predict spatial and temporal variations in stress, strain and contact area/forces (Weiss 2005). Three-dimensional FE modeling of ligament behavior is complicated by non-linear material behavior and complex geometry and boundary conditions. The following section will address previous work done to overcome each complication.

2.2.1 Material Behavior

Structurally, ligaments are composed of a collagen fibers embedded in ground substance matrix of proteoglycans, glycolipids and water. The fiber orientation generally represents an adaptation to the mechanical environment of the ACL, and has been accepted to be highly aligned with the long axis (Zhang 2008). The collagen fibers provide the primary resistance to tensile loading, but provide negligible resistance to compression (Zhang 2008, Limbert 2001, Weiss 2001). The stress-strain curve for ligaments possesses a toe region for uniaxial loading along the fiber direction. One theory to explain the toe region is the sequential recruitment of collagen fibers. As the ligament is stretched, additional fibers are recruited and when a critical stretch is reached all fibers are recruited and the stress-strain behavior becomes linear (Comninou 1976). A typical load-deformation plot of uni-axial loading of ACL along the fiber direction is shown in Figure 7 (Martin 1998).

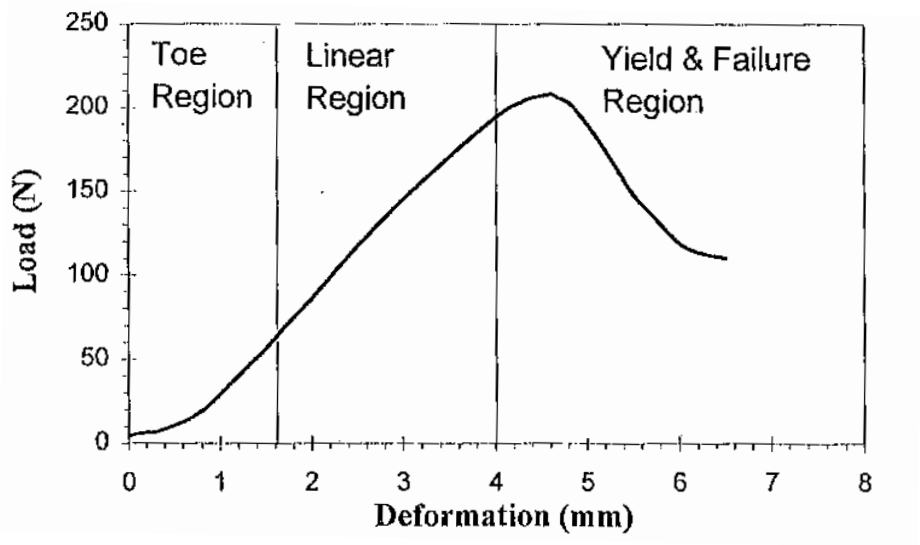

Figure 7: Stress vs. Strain for uni-axial loading of ACL along fiber direction

In addition to the non-linear elastic response, ligaments exhibit time and history dependent visco-elastic properties that arise from the interaction between the water and the ground substance matrix. There have been numerous experimental investigations into the visco-elastic properties of ligaments, as well as attempts to characterize these properties with models (Pioletti 1998, Pena 2006, Duenwald 2009). The results of experimental studies have concluded that the material response of ligament if relative insensitive to strain rate over several decades of variation (Woo 1993, Pioletti 1998). In addition, ligaments reach a pre-conditioned state after repeated loadings, and there is minimal amount of hysteresis (Weiss 2001). Therefore, the inclusion of visco-elastic properties will be neglected and the focus will be on the non-linear elastic response.

Three-dimensional continuum models have been developed to represent the material behavior of ligaments through constitutive equations. Constitutive equations are used to describe the stress-strain behavior of materials through specification of the dependence of stress on variables, such as the deformation gradient, rate of deformation and temperature. The accurate description and prediction of the three-dimensional mechanical behavior of ligaments remains a challenge. Typically, a phenomenological approach, which is mainly concerned with fitting mathematical equations to experimental data, has been used to describe the material behavior of the ACL. One such approach characterizes ligament as a hyperelastic material.

A hyperelastic material postulates the existence of a Helmholtz free energy function, $\boldsymbol{\Psi}$. For the case in which the Helmholtz free energy is solely a function of the deformation gradient, **F**, or some strain tensor, the Helmholtz free energy function is referred to as the strain-energy function. A hyperelastic material is defined as a subclass of an elastic material, where the Cauchy stress tensor is given by (Holzapfel 2000):

$$\boldsymbol{\sigma} = J^{-1}\frac{\partial \Psi(\mathbf{F})}{\partial(\mathbf{F})}\mathbf{F}^{\mathrm{T}} \tag{2.1}$$

For an isotropic hyperelastic material, the strain-energy function can be expressed solely by the principal strain invariants of the right-Cauchy-Green tensor:

$$\Psi = \Psi[\, I_1(\mathbf{C}),\ I_2(\mathbf{C}),\ I_3(\mathbf{C})\,] \tag{2.2}$$

Using the definition of the second Piola-Kirchoff stress:

$$\mathbf{S} = 2\frac{\partial \Psi(\mathbf{C})}{\partial \mathbf{C}} \tag{2.3}$$

and the Piola transformation $\boldsymbol{\sigma} = J^{-1}\mathbf{F}\mathbf{S}\mathbf{F}^{T}$, the Cauchy stress can be written as (for incompressible material):

$$\boldsymbol{\sigma} = \mathbf{F}\left(2\frac{\partial \Psi(\mathbf{C})}{\partial \mathbf{C}}\right)\mathbf{F}^{T} \tag{2.4}$$

Different forms of the strain-energy function have been widely studied and have been shown to represent experimental data well. Pioletti (1998) developed an isotropic viscoelastic constitutive law for ligaments in conjunction with an elastic potential developed by Veronda and Westman (1970) originally proposed to model finite deformations of the skin. In that study, the strain energy function was split into an elastic potential, W_e and a viscous potential, W_v which can be seen in equations 2.5 and 2.6.

$$\boldsymbol{W_e} = \alpha \exp\left[\beta(\boldsymbol{I}_1 - 3)\right] - \frac{\alpha\beta}{2}(\boldsymbol{I}_2 - 3) \tag{2.5}$$

$$\boldsymbol{W_v} = \frac{\eta}{4}\boldsymbol{J}_2(\boldsymbol{I}_1 - 3) \tag{2.6}$$

Where α and β are elastic parameters and η is a viscous parameter. I_1 , I_2 are the first and second strain invariants and J_2 is the second strain rate invariant. Elastic parameters were determined from curve fitting experimental data obtained from the human ACL. The results of the study showed good correlation between experimental and theoretical curves over a range of strain rates and up to 13.5% strain. One significant limitation of this study was the assumption of isotropy. A more comprehensive model would incorporate transverse isotropy, which is more appropriate for ligaments (Pioletti 1998).

More recent studies have suggested the use of a transversely isotropic fiber reinforced material model, where it is assumed that the strain energy function could be split into the sum of a strain energy function representing the mechanical response of the ground substance and a strain energy function encompassing the anisotropic behavior introduced by the collagen fibers (Weiss 1996, Limbert 2001, Song 2004, Zhang 2008). Limbert (2001) represented the ACL as a transversely isotropic hyperelastic material model whose strain energy function took the following form, which was originally developed by (Weiss 1996).

$$\boldsymbol{W} = \boldsymbol{F}_1(\tilde{\boldsymbol{I}}_1) + \boldsymbol{F}_2(\tilde{\lambda}) + \frac{\boldsymbol{K}}{2}\ln(\boldsymbol{J})^2 \tag{2.7}$$

Where the strain energy function was split up in contributions from the ground substance, F_1 and the fibers, F_2 and was uncoupled to deviotoric and volumetric components. $\tilde{\boldsymbol{I}}_1$ is the first deviotoric invariant of the deformation tensor, $\tilde{\lambda}$ represents the deviotoric part of stretch along collagen fiber direction, K is the bulk module and J is the determinant of the deformation tensor. In this model, the ground substance was modeled as incompressible and isotropic and was regarded as a Neo-Hookean model whose strain energy function was described as:

$$\boldsymbol{F}_1 = \frac{1}{2}\boldsymbol{C}_1(\tilde{\boldsymbol{I}}_1 - 3) \tag{2.8}$$

Since the collagen fibers don't support compressive load, and the tensile stretch relationship could be characterized by piecewise continuous function that included a toe region followed by a

linear region, which was only defined for stretch values greater than 1, which can be seen in equation 2.9.

$$\boldsymbol{F}_2(\tilde{\lambda}) = \int \frac{\partial \boldsymbol{F}_2}{\partial \tilde{\lambda}} d\tilde{\lambda} \text{ such that } \begin{cases} \dfrac{\partial \boldsymbol{F}_2}{\partial \tilde{\lambda}} = 0 & \text{if } \tilde{\lambda} \le 1 \\ \dfrac{\partial \boldsymbol{F}_2}{\partial \tilde{\lambda}} = \dfrac{\boldsymbol{C}_2}{\tilde{\lambda}} [\boldsymbol{e}^{\boldsymbol{C}_3(\tilde{\lambda}-1)} - 1] & \text{if } \tilde{\lambda} > 1 \end{cases} \tag{2.9}$$

Where C2 is a factor that scales the exponential stress and C3 controls the rate of un-crimping of collagen fibers. This model matched well with experimental results obtained from passive path kinematics and has since been adopted by other investigators (Song 2004)

2.2.2 Complex Geometry and Boundary Conditions

Perhaps the primary motivating factor to implement FE methods when modeling ligaments is the complex geometry of the ligament and complex boundary conditions that are present in physiology. Zhang (2008) studied the effect of geometry and fiber bundle orientation on finite element modeling of the ACL. The study compared two different geometries and fiber bundle orientations: 1) Realistic and 2) Artificial which can be seen in Figure 8.

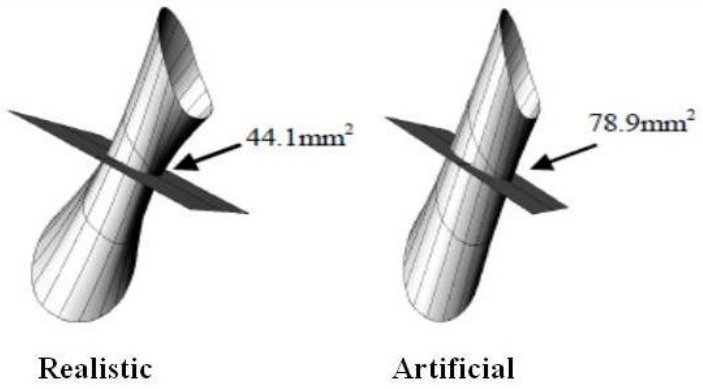

Figure 8: Realistic and Artificial ACL geometry

The artificial geometry is one that is obtained by assuming the ACL has a constant cross section throughout the length, whereas, the realistic geometry was obtained by digitizing the fiber bundles of the ACL and using cubic spline interpolation to fill the remaining geometry. The results of the experiment suggests that the graft force in the realistic geometry and fiber bundle orientation more closely matched experiment, and the un-realistic geometry resulted in a significantly higher peak force during anterior tibial translation (Zhang 2008).

Pena (2005) studied the effect that graft stiffness and graft tensioning had on the stress distribution in an ACL reconstructed knee. Geometry of the bone and ligament graft, as well as the meniscus was obtained from magnetic resonance imaging (MRI). The graft was a patellar tendon which included bone plugs attached at the ends, which can be seen in Figure 9. ATT was measured in response to a 134 anterior tibial load and compared to published results obtained from experiment. The results showed a good correlation between model predictions and published experimental results.

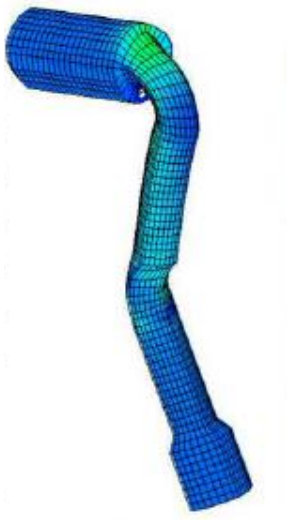

Figure 9: Graft model including bone plugs

In most studies recent studies, the kinematic data used as input to the computational model was obtained experimentally from a knee simulator or a robotic testing system (Zhang 2005, Xie 2009). However, the method for connecting ligament to bone has been debated. Song (2004) studied the interaction between the PL and AM bundles of the DB ACL as well as the effect of ACL wrapping on bone had on ligament force. The insertion surfaces on the ligament were treated as rigid and were bonded to the insertion surface of the bone. The contact between the bone and ligament was treated as a Coulomb friction model. The results of the model suggest that the contact force between the two bundles was insignificant, while the contact force between the bundles and the bone due to wrapping was significant, roughly 10% of the total ACL force.

3.0 EXPERIMENTAL METHODS

3.1 ROBTIC TESTING SYSTEM

Biomechanical testing was performed through the use of a robotic testing system with a universal force sensor (UFS) capable of measuring forces and moments in all 6-DOF. The robotic/UFS testing system has been used for over a decade to study knee kinematics and in-situ forces in the ACL (Darcy 2006). The robot is a six- joint position controlled product (CASPAR Saubli RX 90, Orto MAQUET Germany) with an end-effector position repeatability of $\pm$ 0.02 mm translation and 0.02° rotation, which can be seen in Figure 10 . The universal-force sensor (UFS Model 4015; JR3 Inc., Woodland, CA) has accuracy of ±0.2 N for force and ±0.1 N m for moments according to the manufacturer.

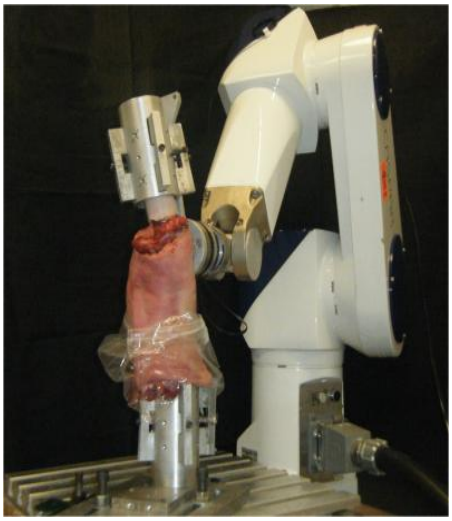

Figure 10: Robotic testing system with knee specimen

3.1.1 Hybrid Control

A hybrid control scheme is used to determine knee kinematics and to control the desired motions. The hybrid control combines aspects of load control and displacement control to achieve a new, "hybrid" method that is better suited to a particular application than either load control or position control alone (Gilbertson 2000). The hybrid control algorithm enables the inherently position-controlled robot to achieve specific load targets in an iterative manner through incrementally applied displacements. At each position along a specified path of motion, the algorithm evaluates the relation between the change in specimen position (i.e. displacement) and the change in UFS-measured loads, and uses this relation to plan the application of the next incremental displacement to achieve the specified load target (Gilbertson 2000). Control is thus based on the *stiffness* of the specimen, which is updated regularly throughout the desired path.

3.1.2 In-situ forces and passive path kinematics

Target forces and moments are the forces and moments desired along a specified path of motion. Passive knee flexion is defined as the motion of the knee that requires very small loads and the target forces and moments are specified to be zero (acceptable limits allow residual forces and moments of 2N and 0.2Nm, respectively) (Rudy 1996). To achieve this passive path, the following procedure is used. First, the user specifies a number of variables, including a user-estimated center of rotation (COR_{est}) and desired flexion angle. Then, the robotic manipulator initially eliminates all residual loads and moments created from securing the specimen to the robotic fixtures, creating a zero load, zero moment equilibrium starting position at full knee extension. Once this equilibrium position is determined, it is stored and the robotic manipulator applies a user specified, in this case 0.5°, increment of flexion ($\Delta R = 0.5°$) about an axis perpendicular to the sagittal plane and passing through the point COR_{est} (x-axis) while the UFS measures the resulting forces and moments. The program then computes the stiffness of the specimen based on the change in UFS-measured loads and the change in position of the tibia (calculated from the change in end-effector position). This stiffness estimate is used to plan the next robotic movement which will reduce any sagittal plane (i.e. superior/inferior and

anterior/posterior) forces that may have resulted from the applied rotational increment ΔR_x. The robot then applies the planned sagittal plane translational displacement to the tibia, and the UFS measures the loads at this new "force-corrected" position. This force minimization loop is repeated for either as many interations as the user specifies, or until sagittal plane forces are minimized below the specified allowable force thresholds. Then, the robotic joint positions and the three-dimensional position of the tibia are stored, along with the UFS-measured loads. The robot then rotates the tibia another $\Delta R_x = 0.5°$ increment about the COR_{est} and the algorithm continues in the same manner until the specified flexion angle has been reached. A flow chart of this passive path algorithm is given in Figure 11.

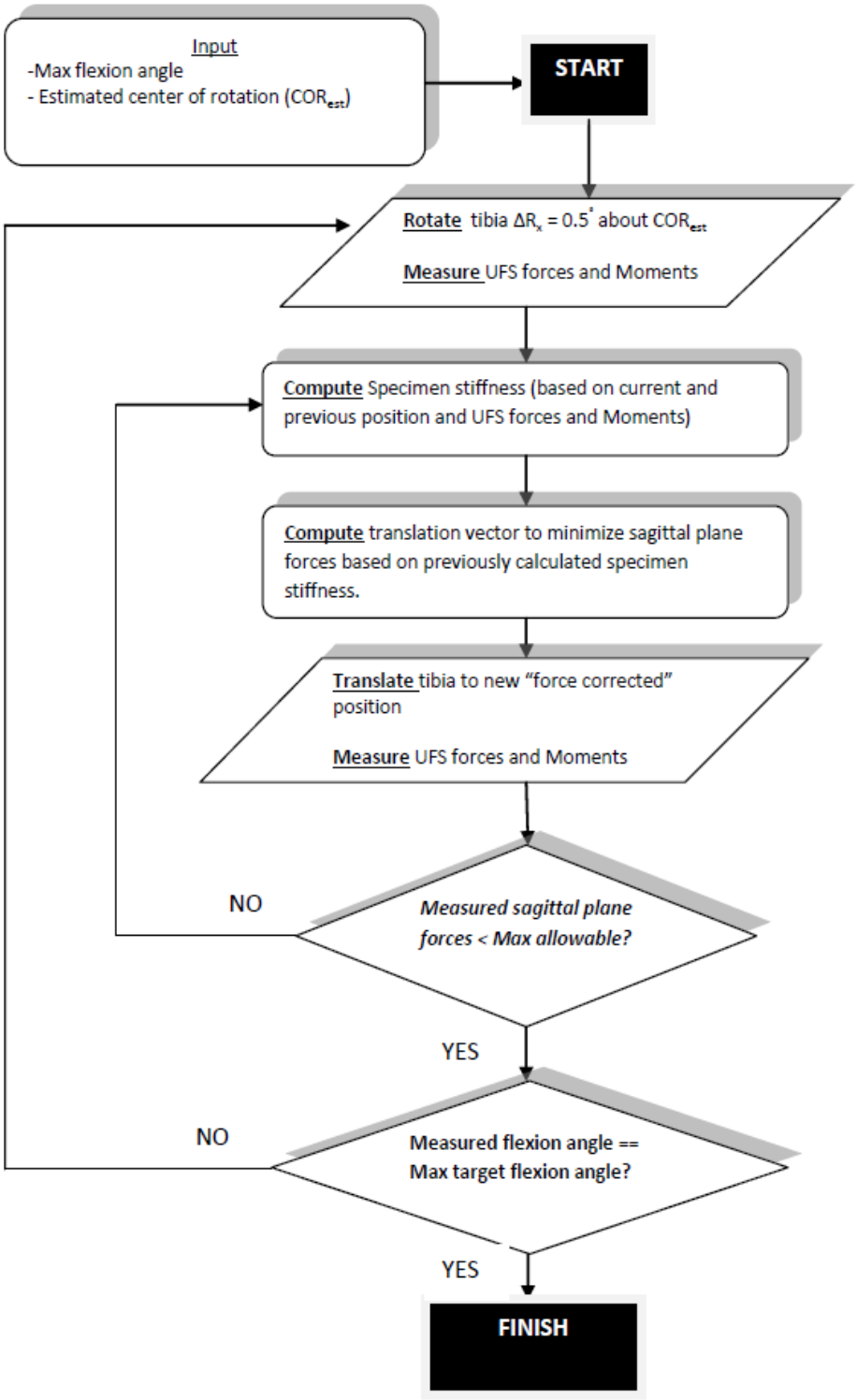

Figure 11: Flowchart of algorithm to determine passive path of flexion

To determine the in-situ force for a specific soft tissue, in this case the ACL, the following procedure is used. First, the passive path of flexion/extension of the knee is found as previously described and the points along that flexion path are usually taken to be starting points (assumed natural position) for an externally applied loading condition. The controller then subjects the specimen to either a specified load (target load) or a specified displacement (target position) determined by the user, and records the position via the robotic manipulator and records forces (F_x, F_y, F_z) via the UFS. The ACL is then cut surgically and the robotic manipulator replays the identical displacements and rotations resulting from the prior loading condition. During this replay of kinematics, the UFS records all new forces (F_{replay_x}, F_{replay_y}, F_{replay_z}). Based on the principal of superposition, the *in-situ* force of the ACL is calculated by taking the difference between the measured force components before and after its removal. The equation used to find the *in-situ* force is shown in Eq. 3.1

$$\boldsymbol{F}_{in-situ} = \sqrt{(\boldsymbol{F}_x - \boldsymbol{F}_{replay\_x})^2 + (\boldsymbol{F}_y - \boldsymbol{F}_{replay\_y})^2 + (\boldsymbol{F}_z - \boldsymbol{F}_{replay\_z})^2} \quad (3.1)$$

3.2 EXPERIMENTAL PROTOCOL

In order to establish an experimental basis for comparison of the computational results, the following experimental procedure was used. Sixteen fresh frozen cadaveric knees were used for the study. Eight (n = 8) were used for the following techniques: 1. Anteromedial bundle reconstruction (AM-AM), 2. Posterolateral bundle reconstruction (PL-PL), 3. Classical vertical SB reconstruction (PL-HighAM), 4. Double bundle reconstruction (DB). The other eight (n = 8) knees were used for anatomical middle position SB reconstruction (MID-MID), so all cases had n=8 specimen samples A 40 N tension was applied to the grafts at a 30° flexion angle and the graft was then rigidly fixed. A schematic of all techniques can be seen in Figure 12.

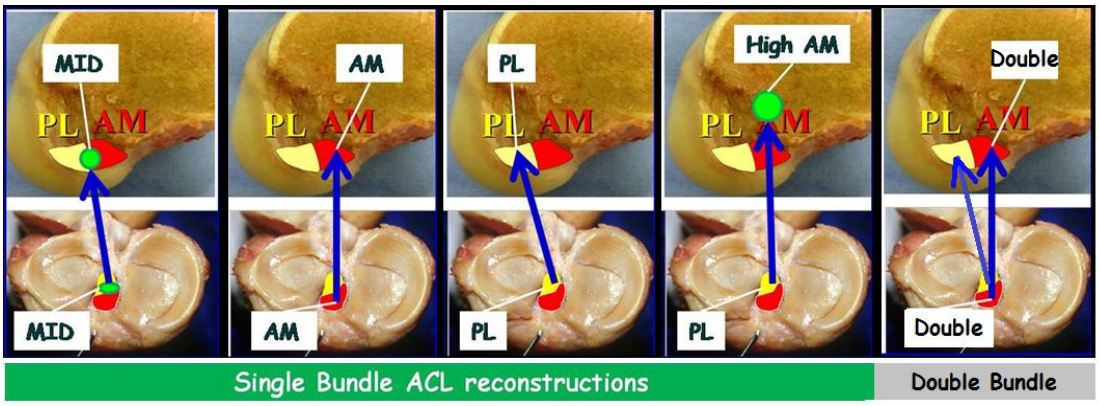

Figure 12: Schematic of five experimental test cases

Each specimen was rigidly secured to the robot with custom aluminum cylinders and an epoxy compound. An anterior load of 89N was applied to the reconstructed knee and the anterior tibial translation (ATT) was recorded at 0, 15, 30, 60 and 90 degrees of flexion. The knee was then removed from the robot and the replacement graft was carefully removed. The knee was then secured back to the robot and the kinematics of the reconstructed state were replayed. An in-situ force vector composed of three dimensional force components in the anterior-posterior, medial-lateral, and superior-inferior directions was then determined, using the method previously

described. A similar protocol was used for each of the five reconstructed techniques to obtain the 3-D force components of the in-situ force vector of the replacement grafts.

3.3 EXPERIMENTAL RESULTS

The magnitude of the in-situ force vector after application of ATT at flexion angles 0°, 15°, 30° 60° and 90° is given in Figure 13.

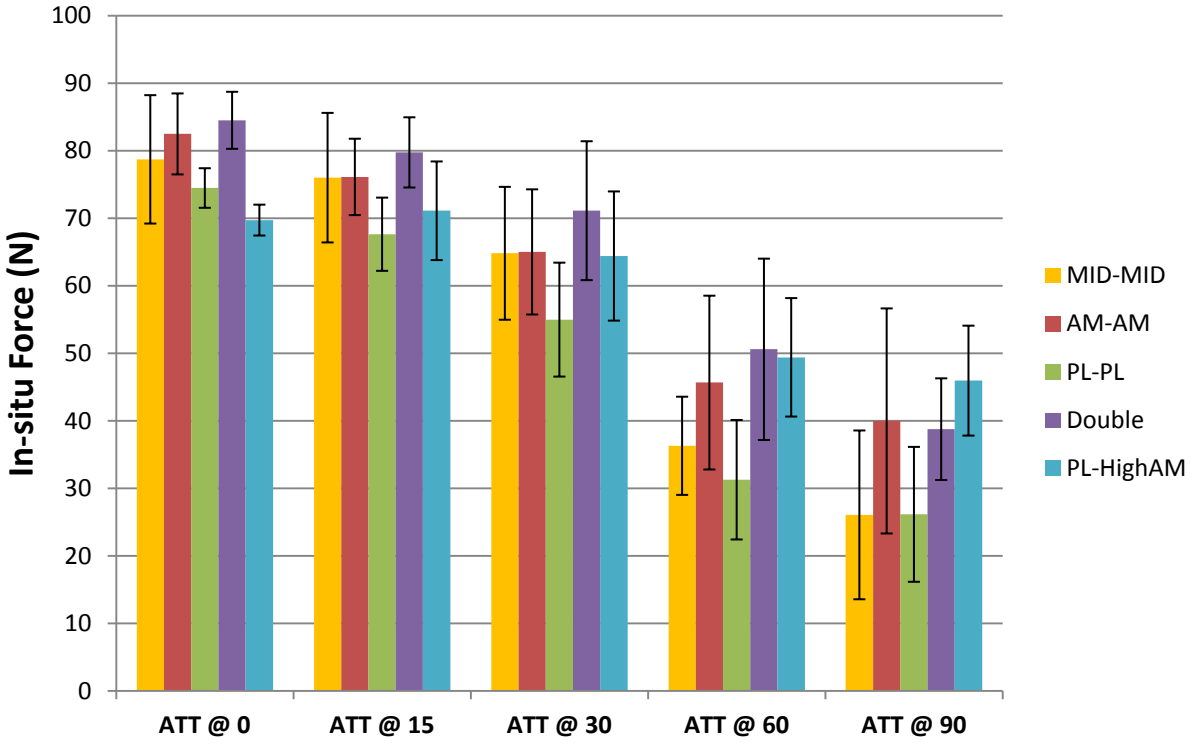

Figure 13: In-situ force of grafts after ATT

From the data it can be seen that the in-situ force of all grafts after ATT tends to decrease as flexion angle is increased. After ATT at 0°, the in-situ force of the PL-High AM graft is the lowest with an average value of 69.7 $\pm$ 2.3N and the in-situ force of the Double bundle graft is the highest with an average value of 84.5 $\pm$ 4.2N. The PL-PL graft had the lowest in-situ force

after ATT at flexion angles of 15°, 30°, 60° and the DB graft had the highest in-site force after ATT at these flexion angles. The variability in the data tends to increase as flexion angle increased. This could be due to either inconsistent graft behavior at higher flexion angles, or inter-subject variability, which is inevitable in human cadaver testing.

4.0 COMPUTATIONAL MODEL

4.1 SOLID MODEL GENERATION

3-D solid models of the tibia and femur were generated from a computer tomography (CT) scan of a human cadaver knee. The CT scans the femur and tibia by slices and captures a digital grey scale image of each slice. The slices were stored as DIACOM (digital imaging and communications in medicine) files. Each slice was 0.6 mm thick and the slices were taken axially along the femur and tibia. The DIACOM data was then post-processed using various digital imaging software packages, which is outlined in the following section.

4.1.1 Bone Modeling

An advanced 3-D imaging and volume modeling program, MIMICS (Materialise, Leuven, Belgium) was used to distinguish and separate bone from soft tissue and generate a 3-D surface model of the femur and tibia. The program took a user defined radiographic density threshold that corresponds to bone to distinguish it from soft tissue. The thresholding and slice spacing of the CT imaging created inherent flaws in the 3-D volumetric model in the form of sharp edges, holes and uneven surfaces. In order to successfully implement a smooth, clean mesh, these surface irregularities needed to be manually repaired. A3-D modeling software, Geomagics Studio (Geomagic, Morrisville, NC*)* was used to patch any holes and smooth sharp edges and surface irregularities. Once surface irregularities were removed, a solid model of the femur and tibia were imported into SolidWorks (Dassault Systemes SolidWorks Corp., Waltham, MA) for further manipulation. Figure 14 shows the completed smooth model of the femur and tibia, in the reference configuration (0° flexion).

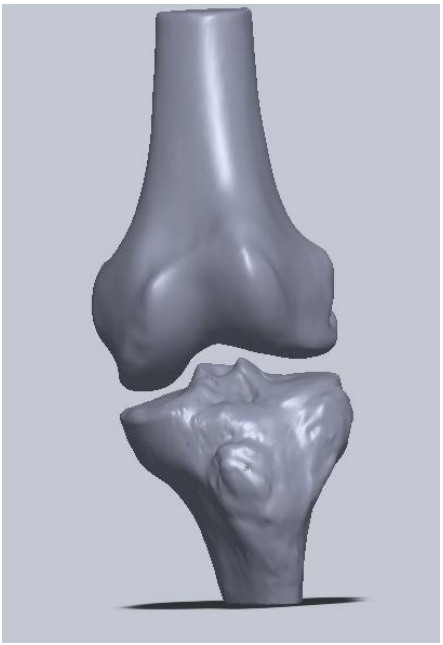

Figure 14: Solid model of tibia and femur in reference position

4.1.2 ACL Modeling

The next task was to generate a 3-D model of the ACL graft from drilled bone tunnels. The bone tunnels were drilled so that they coincided with the insertion sites of the native ACL bundles as well as the tunnel position that results from a transtibial technique previously described, termed PL to High Anterio-Medial (PL-HighAM). Four single bundle ACL reconstructions and one double bundle ACL reconstruction were modeled: 1) PL-PL, 2)AM-AM and 3)PL-HighAM, and 4) MID-MID representing the three single bundle reconstruction techniques and a combination of PL-PL and AM-AM to represent the DB technique. The MID-MID tunnel positions were defined as the geometric mid-point between the centers of the AM and PL bundles. Since the exact geometry of the grafts is unavailable, the corresponding tunnel positions on the tibia and femur were joined with a 6mm diameter solid circular cylinder to represent the graft. Figure 15 illustrates the various tunnel positions used to create the models and Figure 16 shows the solid bodies connecting them. Once the solid models were developed they were loaded into ANSYS (ANSYS Inc. Cannonsburg, PA). This process is outlined in the following section.

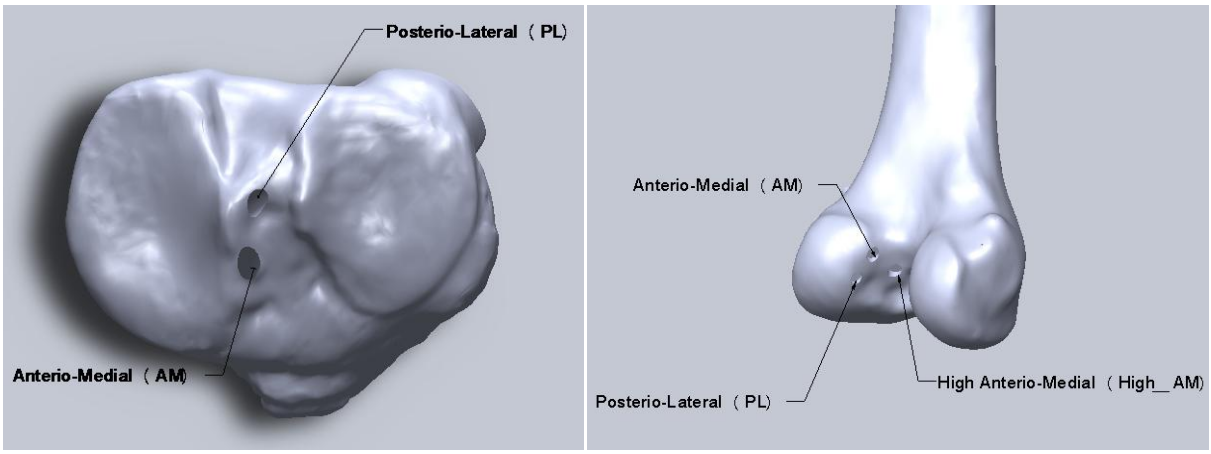

Figure 15: Tunnel insertion sites used for graft placement

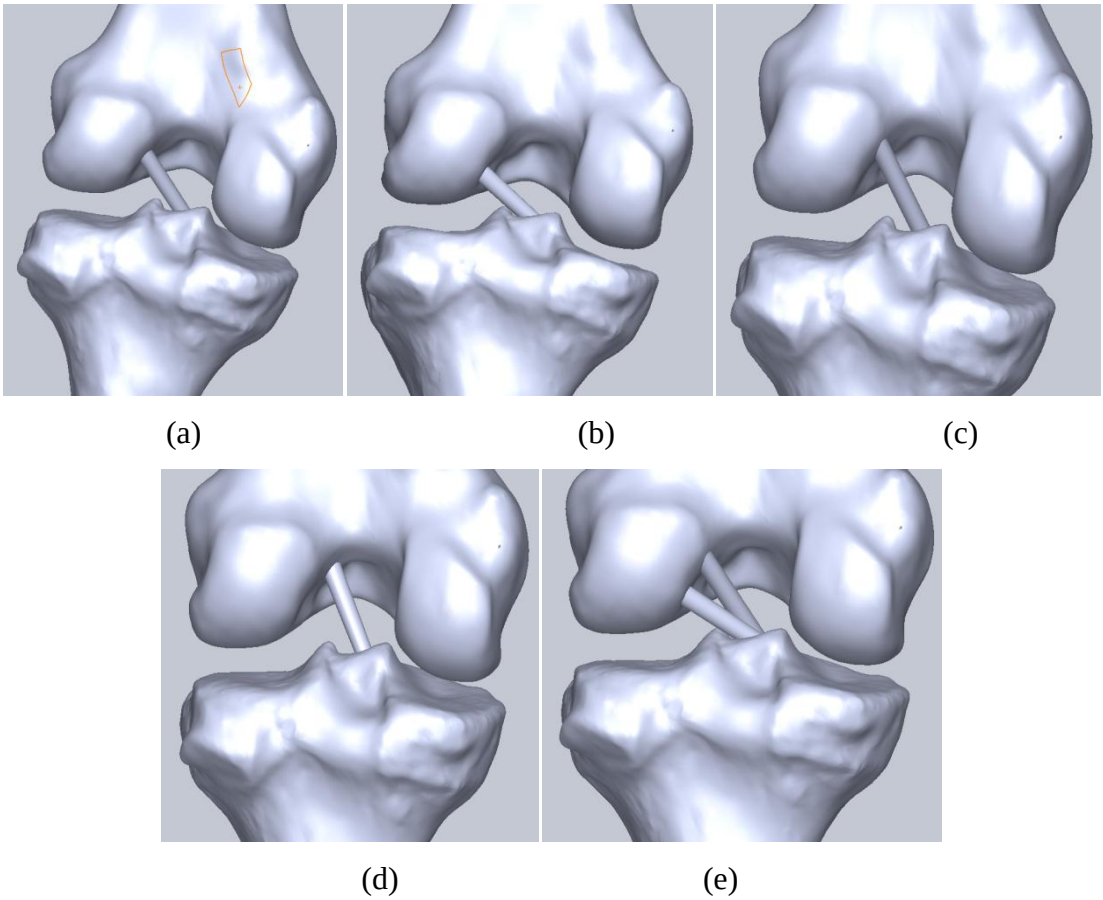

Figure 16: Graft models: (a) Mid-Mid, (b) PL-PL, (c) AM-AM, (d) PL-High AM, (e) DB

4.2 FINITE ELEMENT ANALYSIS

Finite element analysis is a widely used computational method that can be used to determine solutions to complex problems where an analytical solution is unobtainable. It divides a complex problem into many smaller, simpler problems that can be solved numerically to obtain the overall solution. The complex problem in this case is the stress in the ACL replacement grafts resulting from the complex 3-D rigid body motion of the tibia relative to the femur. The geometry of the graft models can be split into a mesh of finite elements, boundary conditions and material properties can be specified, and the software, ANSYS, can provide an approximate solution for the stress and strain of each element and each node.

4.2.1 Mesh generation

The solid model of the tibia and femur were loaded into ANSYS along with the corresponding ACL graft model. The tibia and femur were treated as rigid, and therefore only required surface meshing, using 4-node quadrilateral elements, at the contact region between the bone and graft model. The ACL was meshed using tetrahedral and hexahedral elements. Special care was taken to bond the insertion surfaces of the ACL with the corresponding insertion surfaces of the tibia and femur, using a bonded surface-surface constraint. Each model was initially meshed with a coarse mesh density and results were computed. After the analysis with the coarse mesh, peak stresses and stress distributions were compared to the same model with a finer mesh to ensure proper convergence. The change in peak stress in all models except the Mid-Mid did not exceed 6.2% when using a finer mesh compared to a coarse mesh. The Mid-Mid graft model had a change in peak stress of 10.8% when using a finer mesh, and had considerable variation in the stress distributions between each mesh density, particularly around the insertion surfaces due to high curvature in this region. Therefore, the refined mesh was used for the Mid-Mid graft model. When meshing the AM-AM graft model a total of 213 tetrahedral solid elements and 416 nodes were used, along with 31 surface elements with 110 nodes on the tibial and femoral contact surfaces. Figure 16 (a) shows the AM-AM model mesh. The PL-PL, PL-High AM and DB graft models were meshed with a similar mesh density and can be seen in Figures 17 (b), 17

(c) and 17 (e), respectively. The Mid-Mid graft model was meshed with a finer density as previously stated and a total of 491 tetrahedral solid elements with 1091 nodes were used, which can be seen in Figure 17 (d). The DB graft model required an extra contact pair between the two grafts since during flexion, the two grafts came in contact with each other. A frictionless contact pair was applied between the two grafts, which was a reasonable estimation based on the small effect friction may have on the total stress.

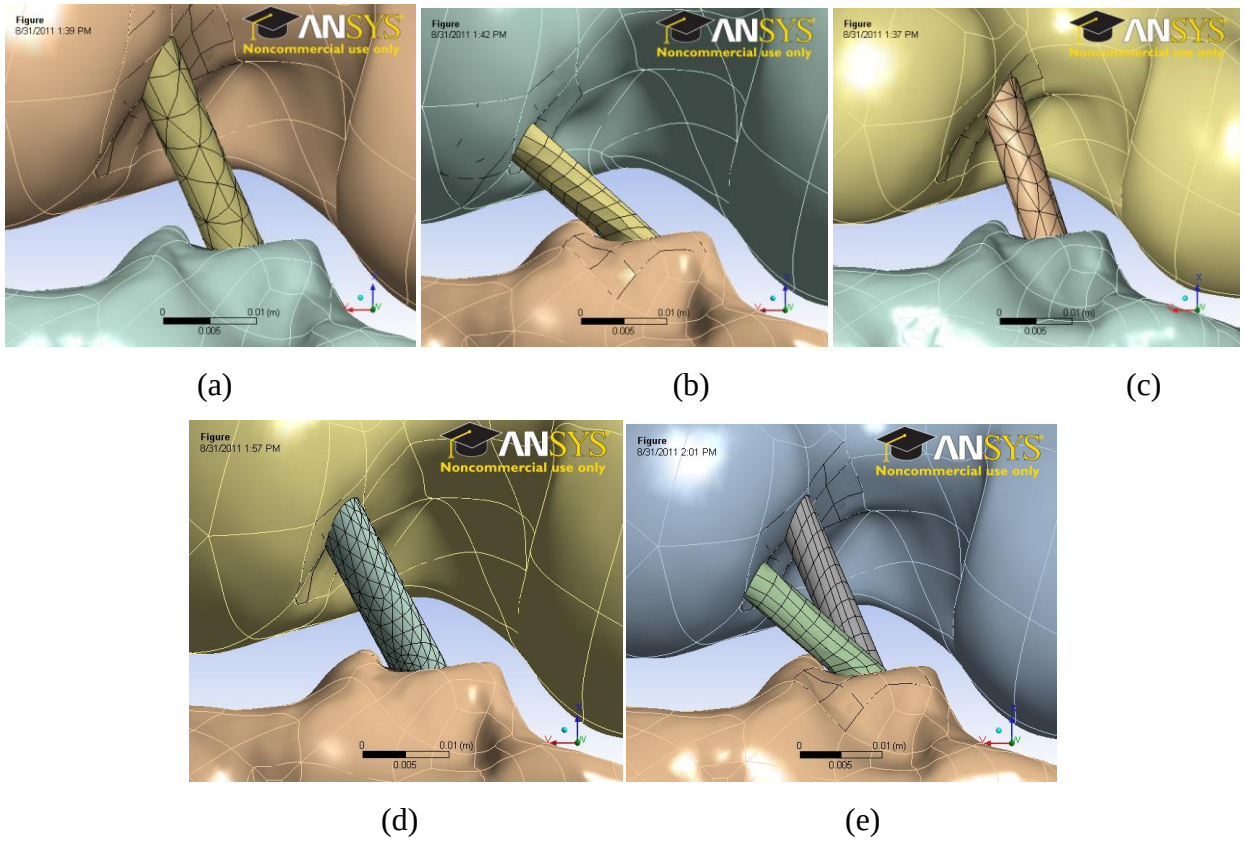

Figure 17: Meshed: (a) AM-AM, (b) PL-PL, (c) PL-High AM, (d) Mid-Mid, (e) DB

4.2.2 Constitutive model of ACL

An elastic strain energy function W_e, for describing incompressible soft tissue behavior was adopted as (Veronda and Westmann, 1970):

$$W_e = \alpha \exp[\beta(I_1 - 3)] + C_1(I_2 - 3) \tag{4.1}$$

The material constants (α,β, C_1) were taken from literature, which had been determined according to the experimentally obtained stress-deformation gradient curve of the human ACL (Pioletti 1998). α=0.26, β= 11.35, C_1= -1.49. In order to directly implement this strain energy function into ANSYS, the form had to be manipulated.

Given $x = I_1 - 3$, the Taylor series expansion of $\alpha \exp[\beta(I_1 - 3)]$ is:

$$\alpha e^{\beta x} = \alpha\left(1 + \beta x + \frac{\beta^2 x^2}{2!} + \frac{\beta^3 x^3}{3!} + \frac{\beta^4 x^4}{4!} + \cdots\right) \tag{4.2}$$

Then, $\alpha = 0.26$, $\alpha\beta = 2.95$, $\alpha\frac{\beta^2}{2!} = 16.74693$, $\alpha\frac{\beta^3}{3!} = 63.3592$. Therefore, in this polynomial form of the strain energy function the coefficients of the first, second and third orders are 2.95, 16.7463, and 63.3592, respectively. This polynomial strain energy function was then implemented into ANSYS as a cubic equation with the coefficients C10 = 2.95, C20 = 16.7463, C30 = 63.3592 and C01 = -1.49. To check to error associated with truncating the Taylor series at 3rd order, equations 4.1 and 4.2 were evaluated at all nodes in the PL-PL model at the end of a full flexion cycle. The average relative error between the model and the Taylor series approximation for the PL-PL model during flexion was 0.49% and the maximum relative error was 7.7%, which was sufficiently small to consider equation 4.2 a valid approximation.

4.2.3 Initial Conditions

Two sets of initial conditions were examined: one, in which the graft was in a stress-free state at full extension and the second, in which the graft was assigned an initial stress that corresponded to a 40N tensile load at full extension. To determine the initial stress field, a 40 N load was applied along the direction of the long axis of each graft model at the tibial interface, while the femoral interface was held fixed. The nodal stresses that resulted were then applied as an initial stress state to determine the effect a 40N initial tension has on graft behavior, when subject to intact knee kinematics. Figure 18 and 19 show the boundary conditions for the determination of the pre-stressed state and the resulting stress distribution, respectively, for the AM-AM model.

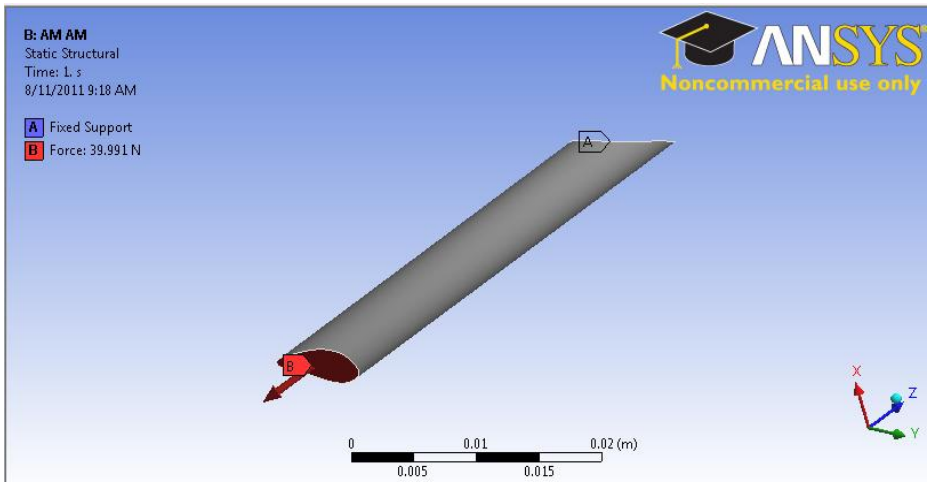

Figure 18: Boundary conditions for determining pre-stress in the AM-AM

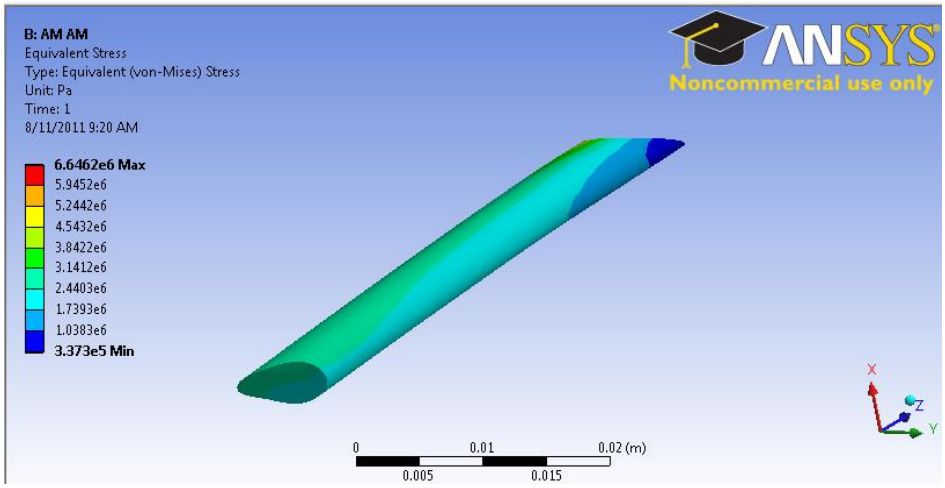

Figure 19: Resulting stress field (Von-Mises) for pre-stress in AM-AM

4.3 THREE-DIMENSIONAL JOINT KINEMATICS

An experimental study of joint kinematics involves the tracking of rigid-body motion of bones in three-dimensions. To measure this motion many different methodologies have been utilized. Stereometric measurement systems use multiple image-gathering devices to triangulate markers in the measurement field (Fisher 2001). These systems can collect data from a large working space but accuracy is limited by the number and placement of cameras and the resolution of images obtained. Magnetic tracking devices use a magnetic field generator and inductive sensors with three orthogonal coils to determine the position and orientation of the sensor with respect to the generator. Mechanical linkage systems incorporate six degrees of freedom and use potentiometers to measure position of linkage joints and determine the end-to-end position and orientation. Most of these techniques utilize a local coordinate system fixed in the body of interest to describe its changing position and orientation with respect to a global reference frame. However none of the methods described has an intrinsic means of relating the object geometry (anatomy) with the local coordinate system (Fisher 2001). In order to correlate the bone geometry and the rigid body motion of the femur and tibia, three aluminum screws were

implanted in the femur and three in the tibia (Fig. 20), thereby allowing the location of the local system within the global CT imaging data sets to be determined. The motion of the bones was captured via a FARO arm spatial digitizer (FARO Technologies Inc. Lake Mary, FL) with positional accuracies of 0.03mm.

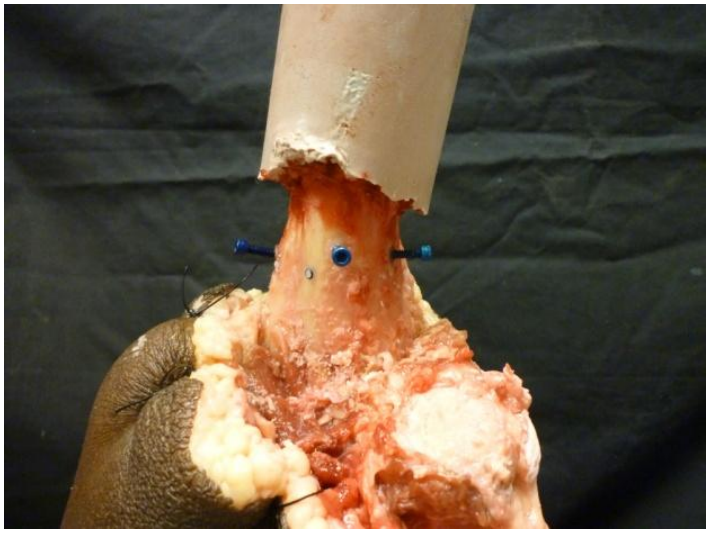

Figure 20: Registration screws implanted in tibia

4.3.1 Registration screws local coordinate system

The position and orientation of a local coordinate system (x, y, z) in a global reference frame (X, Y, Z) (Fig. 21) can be entirely described by the global position of the local coordinate system origin and global description of the three orthogonal unit vectors (**i, j, k**) that represent the axes of the local coordinate system (Fisher 2001).

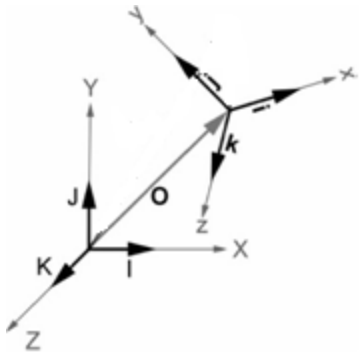

Figure 21: Local coordinate system (x, y, z) defined with respect to the global reference frame (X,Y,Z)

The registration screw's local coordinate system origin is based off of the centroid of a 3mm glass ball glued to the end of the hexagonal head. A 3mm glass ball was used to match the dimensions of the tip of the FARO arm spatial digitizer and to ensure that the ball could be seen in a CT image.

To create a local orthogonal coordinate system, two unit vectors connecting the origin to the remaining two screw's centroids were defined. The cross product of these two unit vectors yielded the first orthogonal axis. The second orthogonal axis could be either one of the original unit vectors, since they are both orthogonal to first axis. The final axis is found by taking the cross product of the first and second orthogonal axis. The result is three orthogonal unit vectors local to the body, but defined in a global reference frame.

The two global measurement systems considered here are the CT reference frame, in which the bone geometry and glass registration balls are viewed in the medical imaging data set, and the FARO arm spatial digitizer reference frame where position and orientation of the bones was measured during the kinematic manipulation. In order to apply the captured kinematics to the bone geometry, a transformation from the global digitizer coordinate system to the global CT coordinate system needed to be made. To do this, two transformation matrices were formed. The first was a transformation from digitizer global to local, $\boldsymbol{T}_{G\to L}^{dig}$

$$\boldsymbol{T}_{G\to L}^{\boldsymbol{dig}} = \begin{bmatrix} 1 & 0 & 0 & 0 \\ \boldsymbol{O}_x & \boldsymbol{l}_1 & \boldsymbol{l}_2 & \boldsymbol{l}_3 \\ \boldsymbol{O}_y & \boldsymbol{m}_1 & \boldsymbol{m}_2 & \boldsymbol{m}_3 \\ \boldsymbol{O}_z & \boldsymbol{n}_1 & \boldsymbol{n}_2 & \boldsymbol{n}_3 \end{bmatrix} \tag{4.3}$$

Here, the values O_x, O_y , O_z correspond to the location of the origin of the digitizers local coordinate system , which was arbitrarily assigned to the centroid of the medial ball and l_i, m_i, n_i are the three calculated orthogonal unit vectors that were found as previously described. The transformation from digitizer local to global coordinate system can be found simply by taking the inverse:

$$\boldsymbol{T}_{\boldsymbol{L\rightarrow G}}^{dig} = inv(\boldsymbol{T}_{G\rightarrow L}^{dig}) \tag{4.4}$$

A similar process was used to define the transformations from global to local in the CT's reference frame, and the transformation matrices were formed, instead termed $\boldsymbol{T}_{G\rightarrow L}^{CT}$ and

$$\boldsymbol{T}_{L\rightarrow G}^{CT} = inv(\boldsymbol{T}_{G\rightarrow L}^{CT}) \tag{4.5}$$

In order to have all data in one common global coordinate system, which was arbitrarily picked to be the CT's since the bone geometry was in the CT's global reference frame, the following transformation was made to the kinematic data obtained from the digitizer, $\overline{\boldsymbol{X}}_{\boldsymbol{i}}^{\boldsymbol{dig}}$

$$\overline{\boldsymbol{X}}_{\boldsymbol{i}}^{\boldsymbol{CT}} = \boldsymbol{T}_{\boldsymbol{L\rightarrow G}}^{\boldsymbol{CT}} \bullet \boldsymbol{T}_{\boldsymbol{G\rightarrow L}}^{\boldsymbol{dig}} \bullet \overline{\boldsymbol{X}}_{\boldsymbol{i}}^{\boldsymbol{dig}} \tag{4.6}$$

4.3.2 Kinematic data

The input displacement data for the computational model was obtained from the robotic testing system. The passive path of the joint was first determined by methods previously described and the location of the three tibial registration screws were digitized at 3° increments from 0° to 90° flexion, while the femur remained fixed. Next, an 89 N anterior force was applied at 0, 15, 30, 45, 60 and 90 degrees of flexion which results in an anterior tibial translation (ATT) and the tibia registration screws were digitized in 0.5 mm increments through the full anterior motion of the

tibia. The kinematic data obtained by the robotic testing system can now be implemented as displacement boundary conditions to the FE model.

4.4 RESULTS OF COMPUTATIONAL MODEL

The 1st principal stress and ligament force were found during flexion and after ATT at flexion angles previously mentioned for all graft models. The distance between the centers of the tunnel insertions as a function of flexion angle was also found.

4.4.1 Change in Distance of Insertion Sites

The kinematics of the tibia relative to the femur of the passive path of flexion/extension from 0° to 90° for a healthy human knee were input into ANSYS as a boundary conditions. First, the distance between insertion sites was determined as a function of flexion angle. The results are shown in Figure 22.

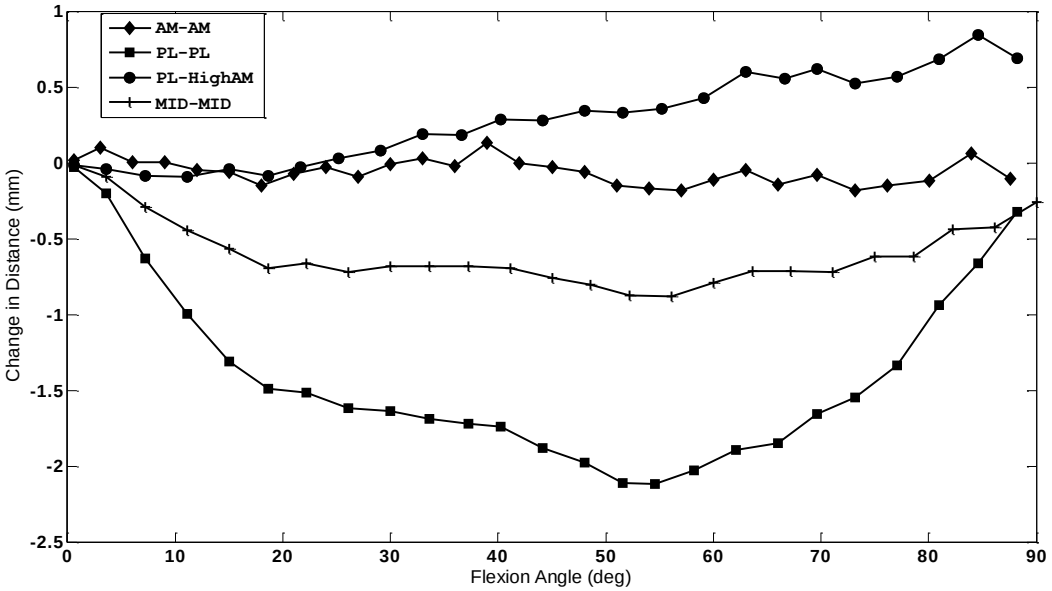

Figure 22: Length change between insertion sites vs. flexion angle

As seen in Figure 22, the distance between the PL-PL graft model insertion sites undergoes the most dramatic length chance, decreasing as a function of flexion angle from 0° to 53°, and then increases steadily back to the original distance. It reaches a peak decrease of 2.11 mm. The distance between the PL-HighAM graft model insertion sites increase as a function of flexion angle from 0° to 90°, to a maximum value of 0.85 mm. The Mid-Mid graft undergoes a length decrease similar to the PL-PL, but less extreme, to a peak decrease of 0.88 mm. The distance between insertion sites of the AM-AM graft model undergoes minimal change, and the length remains relatively constant throughout the passive path of flexion/extension. The DB graft model was excluded here since it is simply a combination of the PL-PL and AM-AM graft models.

4.4.2 Stress-free Initial Condition

The stress-free initial condition was defined as all graft models having a stress-free initial condition at 0° flexion. The graft tension and stress results are summarized in the following sections.

4.4.2.1 Graft Tension Figure 23 shows the graft tension as a function of flexion angle. The tension in the graft was determined from the reaction forces at the graft-tibia interface. The component of the reaction force that was parallel to the long axis of the graft was considered the graft tension. The long axis of the graft was a unit vector that connected the centroids of the graft-bone interface surface. For the DB case, the components of the force reactions of the PL-PL and AM-AM grafts were added and the resulting sum was the total force reaction.

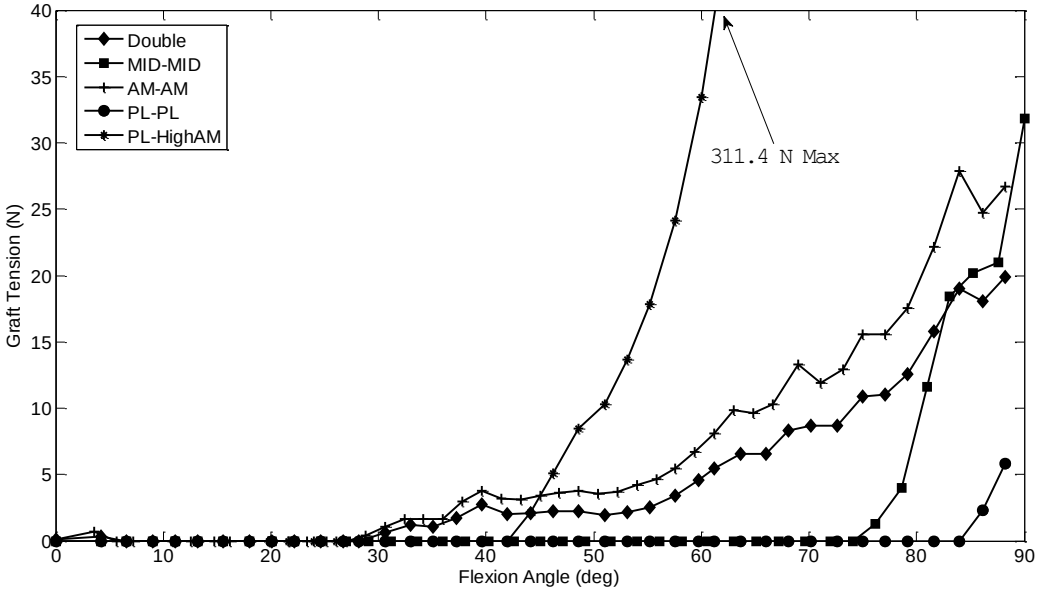

Figure 23: Graft tension vs. flexion angle for stress-free initial condition

As seen in Figure 23, the DB and AM-AM graft models both initiate tension at 24° and reach maximum values of 19.8 N and 25.2 N, respectively. The Mid-Mid and PL-PL graft models initiate tension at 76° and 84° and reach maximum values of 31.9 N and 11.6 N, respectively. The PL-HighAM graft model initiates tension at 36° and increases dramatically to a maximum value of 311.4 N (partially excluded for clarity), an order of magnitude higher than any other graft model. Figure 24 shows the tension in the graft after application of the 89N anterior tibial (ATT) load at 0°, 15°, 30°, 45°, 60°, and 90° flexion for the stress-free initial condition.

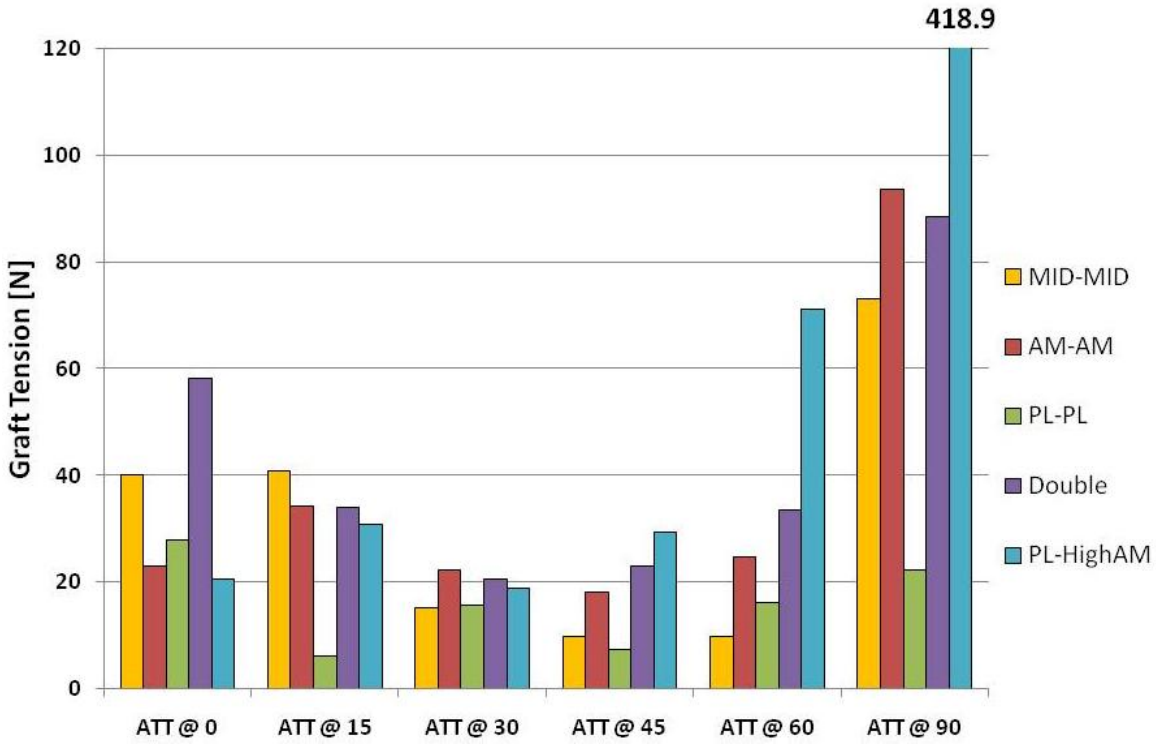

Figure 24: Graft tension after ATT for stress-free initial condition

As seen in Figure 24, the tension in the PL-PL graft model is the lowest of all models after the ATT load at flexion angles of 15°, 45° and 90° with the lowest value of 7.9N at 15°. The tension in the PL-High AM model remains relatively constant after ATT load at flexion angles of 0°, 15°, 30° and 45° and then increases dramatically at 60° and 90° of flexion to 71.1N and 418.9 N, respectively. The DB graft model has the highest graft tension after ATT at 0°, with a value of 58.3N. The Mid-Mid and AM-AM graft models follow similar trends, with lowest tension occurring at 30°, 45° and 60° and a dramatic increases at 90° to maximum values of 73.1 N and 93.6N, respectively.

4.4.2.2 Stress Analysis The 1st principal stress in the grafts during flexion extension was determined. In all cases, the maximum stress occurred at the insertion sites on the tibia and femur due to the stress concentrations that arise. Since the true boundary conditions cannot be adequately modeled here, the stresses at or near the bone-graft interface will be ignored and the values reported are for nodes at locations 10% of the total length from each respective insertion

site, or nodes in the middle 80% of the graft. Maximum stress (1st principal) in the single bundle grafts, with a zero pre-stress at 0°, during flexion extension can be seen in Figure 25. Figure 26 compares the peak stress in the AM-AM and PL-PL bundles when they are modeled solely (SB) and when they are combined to form the DB model for the case of zero pre-stress**.**

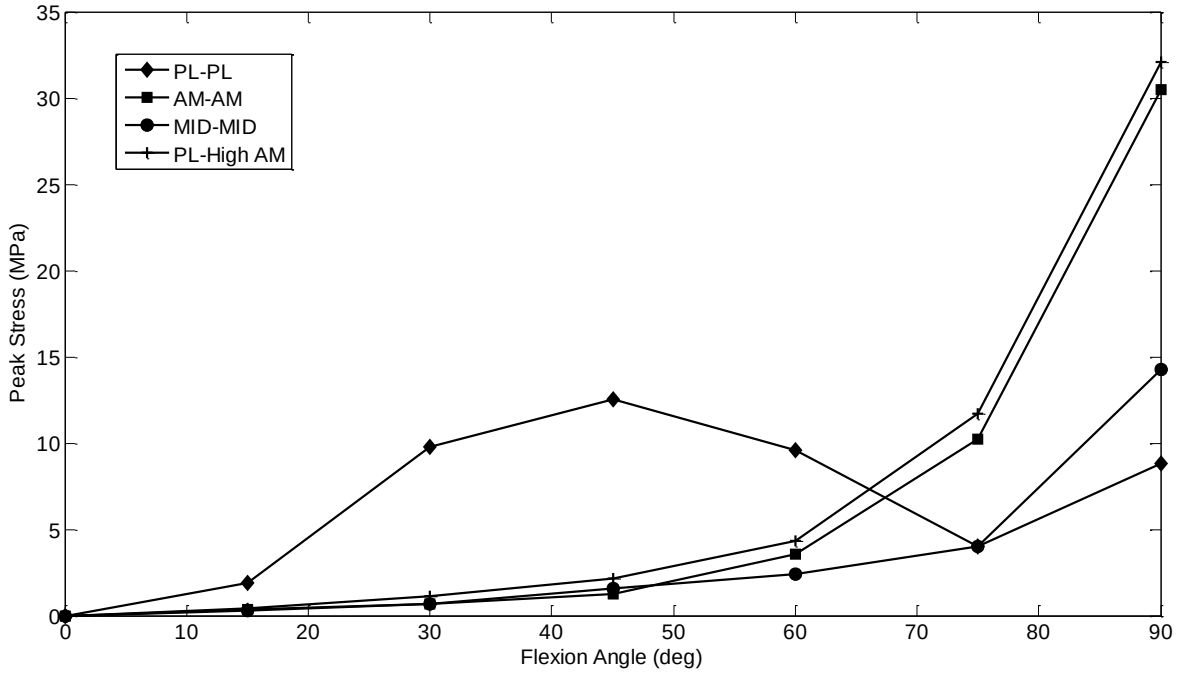

Figure 25: Peak stress vs. flexion angle for SB models for stress-free initial condition

As seen in Figure 25, the peak stress in the PL-PL graft model increases as flexion angle increases until 45° flexion, with a maximum value of 12.5 MPa, respectively. Conversely, the stress in the AM-AM and PL-HighAM graft models show lower peak stress at low flexion angles until a dramatic increase at approximately 60° flexion to a maximum value of 30.3 MPa for the AM-AM and 32.1 MPa for the PL-High AM graft models. The stress in the MID-MID graft model increases slowly as a function of flexion angle to a maximum value of 14.3 MPa at 90° flexion.

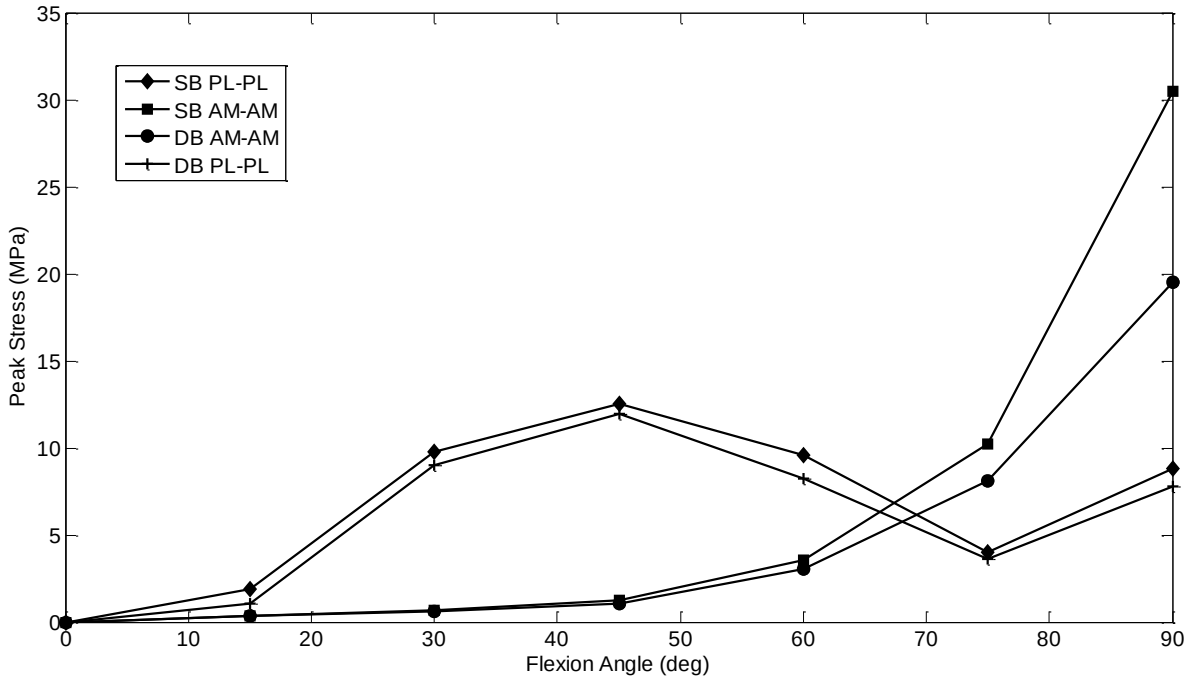

Figure 26: Peak stress vs. flexion angle for SB and DB bundles for stress-free initial condition

As seen in Figure 26, the peak stress in the AM-AM and PL-PL models follow similar trends regardless of whether they are treated solely or as a combination. However, the peak stresses in the grafts decrease when they are modeled in combination. The maximum stress in the PL-PL graft decreases by 5.6% from 12.5 MPa to 11.8 MPa at 45° and the maximum stress in the AM-AM graft decreases by 35.3% from 30.3 MPa to 19.6 MPa at 90°. Figures 27-31 show contour plots of the stress distribution in each graft model at flexion angles of 30°, 60°, and 90°. The white areas indicate compressive stresses. Figure 32 shows the contact pressure between the AM-AM and PL-PL bundles in the DB graft model.

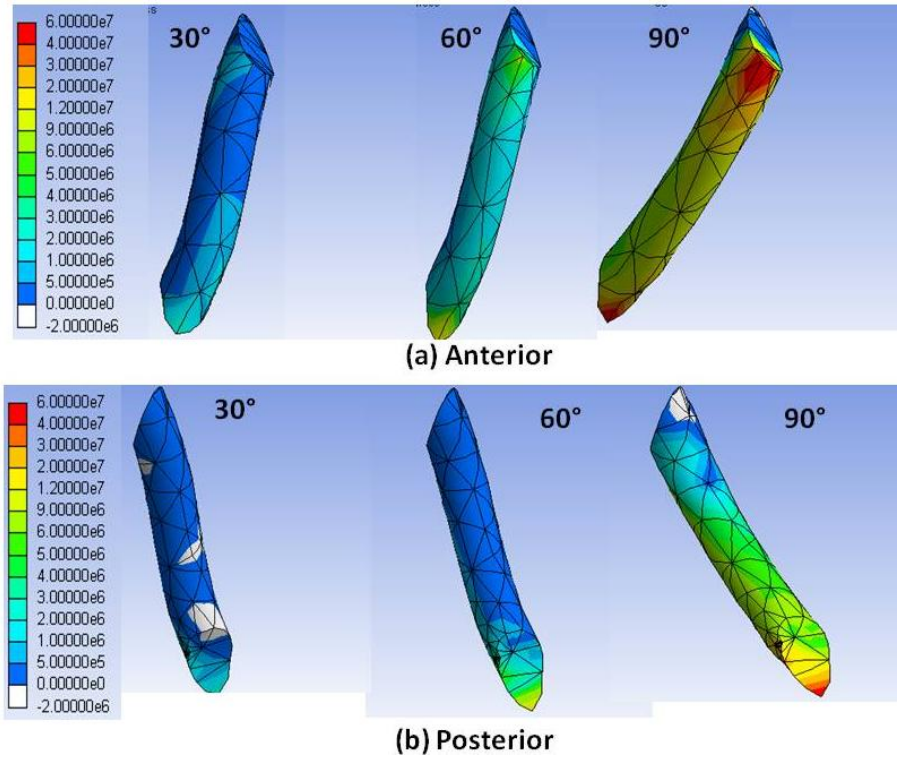

Figure 27: Stress distribution in the AM-AM during flexion for stress-free initial condition

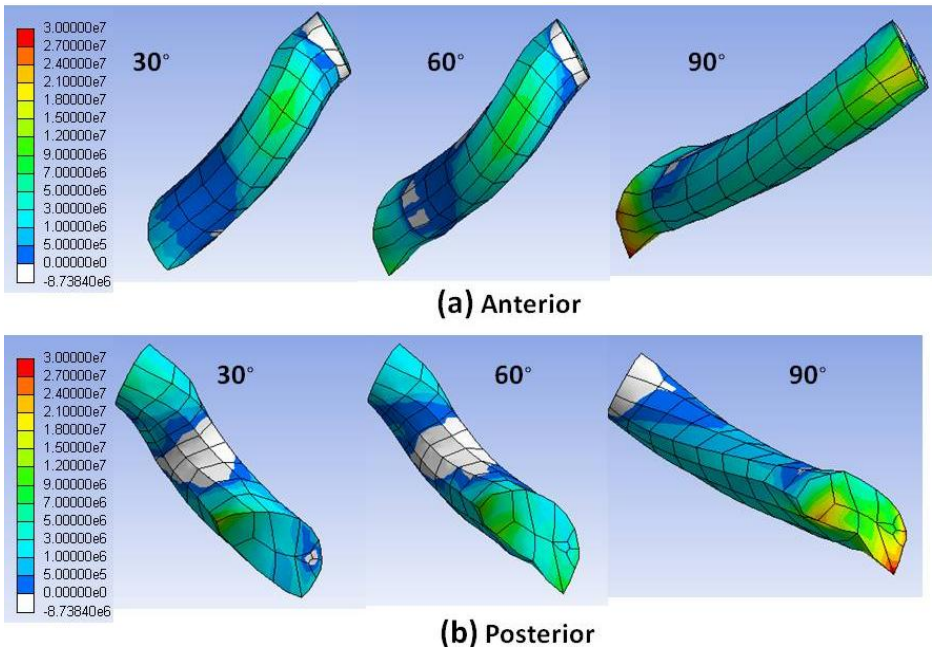

Figure 28: Stress distribution in the PL-PL during flexion for stress-free initial condition

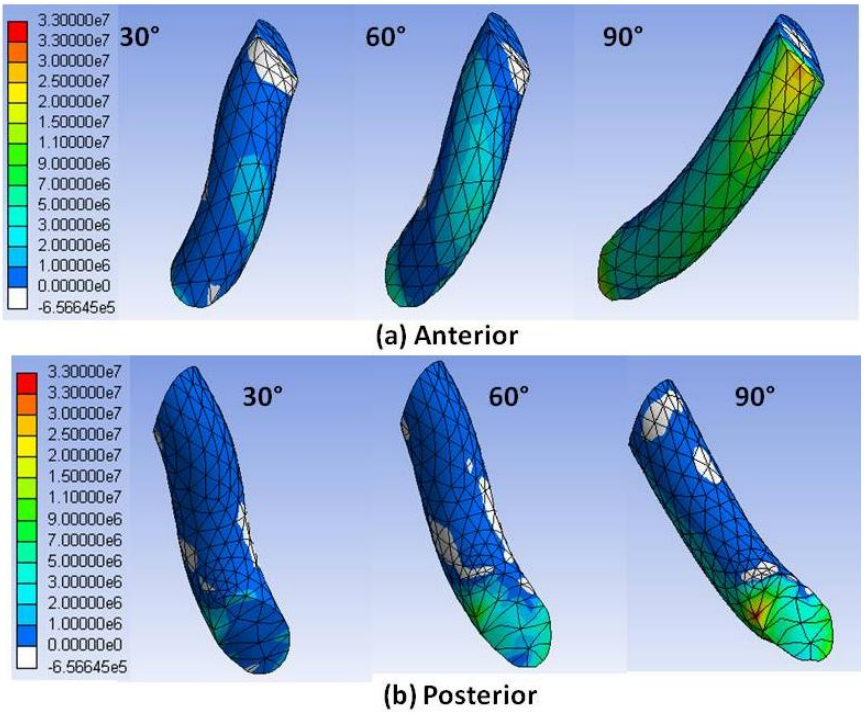

Figure 29: Stress distribution in the Mid-Mid during flexion for stress-free initial condition

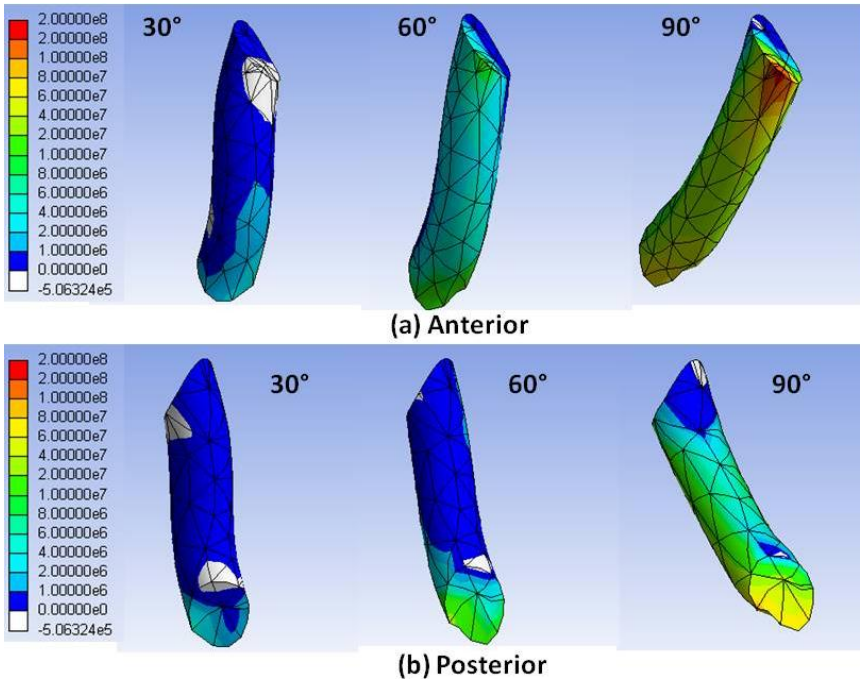

Figure 30: Stress distribution in the PL-High AM during flexion for stress-free initial condition

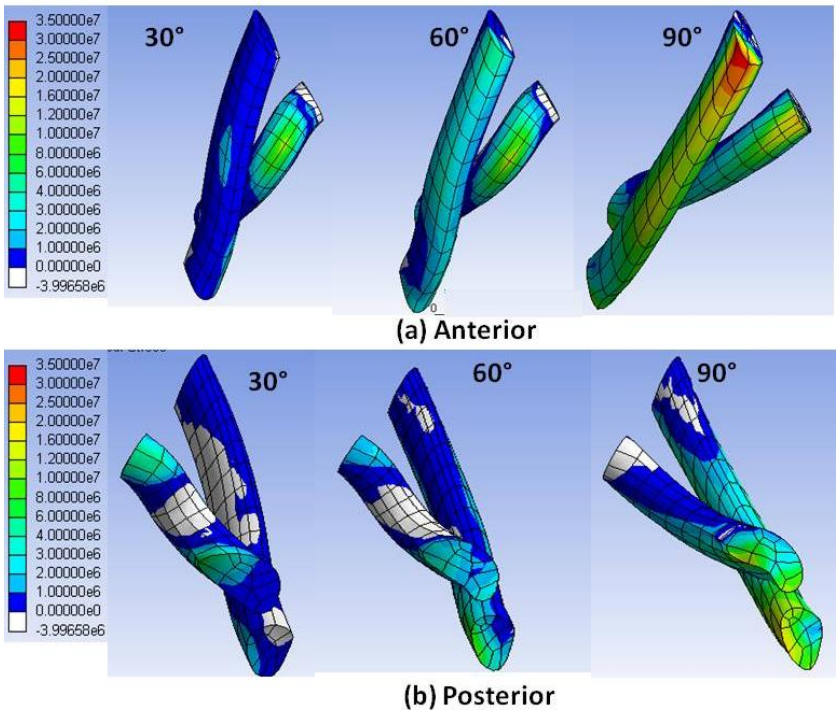

Figure 31: Stress distribution in the DB during flexion for stress-free initial condition

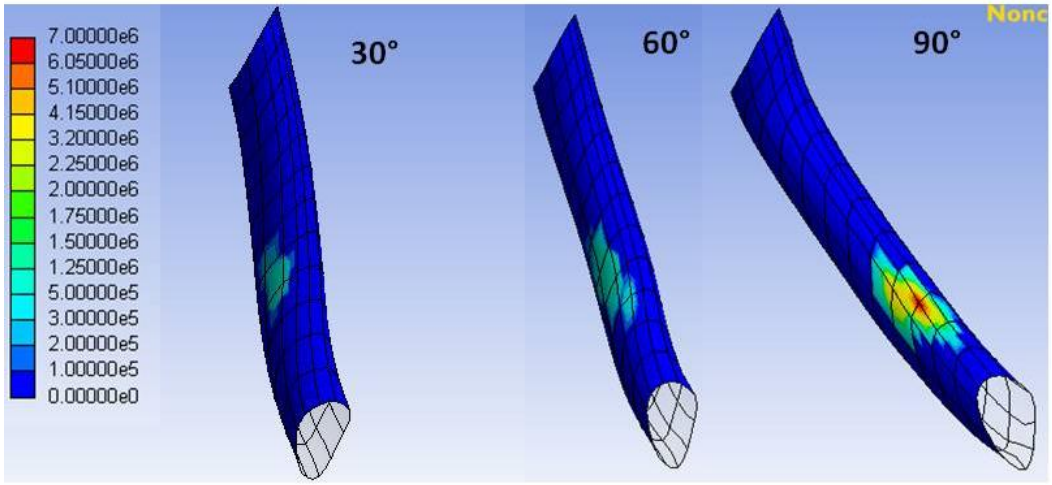

Figure 32: Contact pressure between AM-AM and PL-PL during flexion for stress-free initial condition

Figure 33 shows the peak stress in all single bundle (SB) graft models after application of the 89N anterior tibial load at flexion angles of 0°, 15°, 30°, 45°, 60° and 90°. Figures 34 and 35 show the peak stress in the AM-AM and PL-PL grafts when analyzed solely (SB) and in combination (DB).

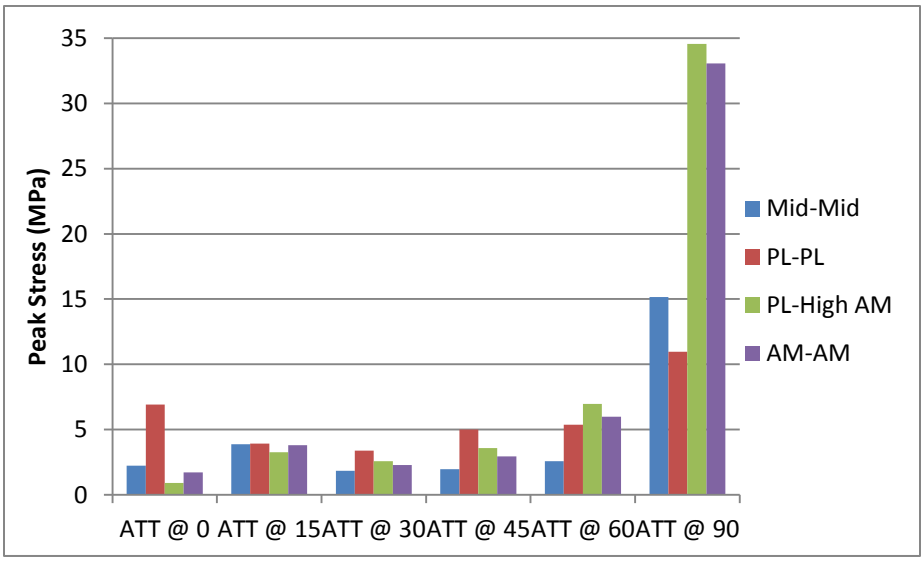

Figure 33: Peak stress in SB models after ATT for stress-free initial condition

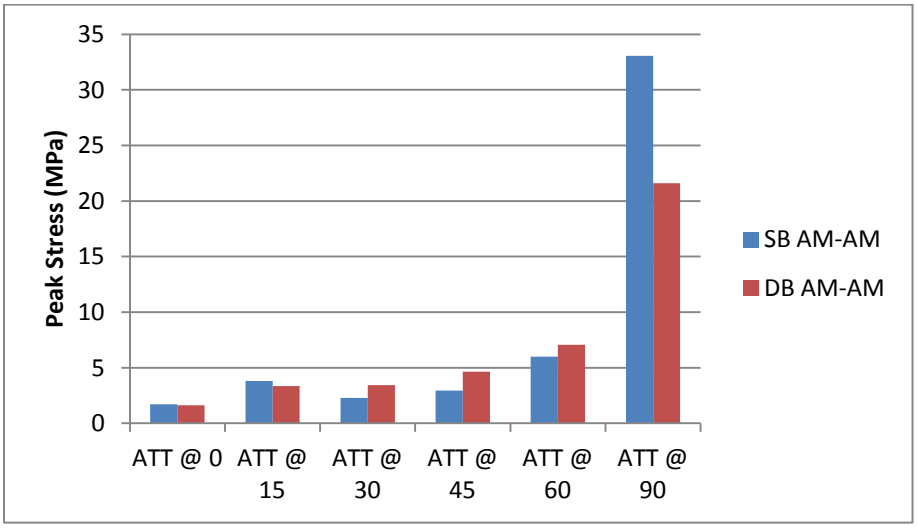

Figure 34: Peak stress in the AM-AM after ATT in SB and DB models for stress-free initial condition

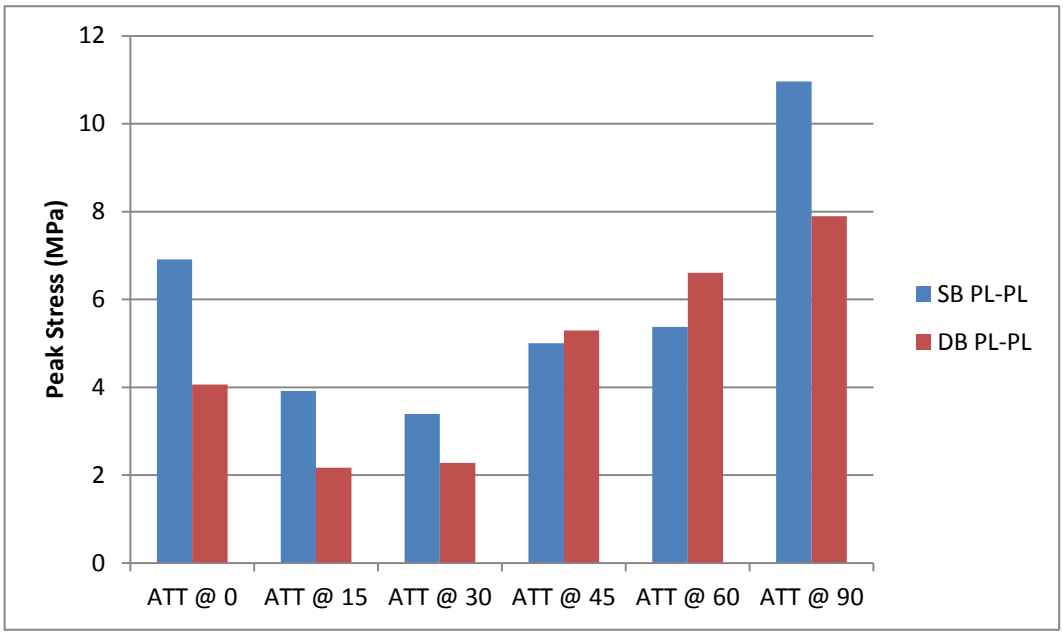

Figure 35: Peak stress in the PL-PL after ATT in SB and DB models for stress-free initial condition

As seen in Figure 33, all SB graft models reach maximum stresses after ATT at 90° flexion. This result is not surprising considering the high stress on the graft resulting from flexion. The PL-High AM graft model has the highest stress, with a maximum value of 34.6 MPa at 90°. The Mid-Mid graft model has the lowest stress among all models after ATT at flexion angles of 15°, 30°, 45° and 60° while the PL-High AM graft model has the lowest stress after ATT at 0° flexion. As seen in Figure 34, the AM-AM graft has similar peak stresses at 0° and 15° when modeled as SB or DB. However, at 30°, 45° and 60° the peak stress in the DB AM-AM model exceeded the SB AM-AM model. At 90°, the peak stress in the DB AM-AM is significantly less than the SB AM-AM. As seen in Figure 35, the peak stress in the DB PL-PL model is significantly less after ATT at 0°, 15°, 30° and 90°. However, at 45° and 60° the peak stress in the DB PL-PL is greater than the SB-PL-PL model. The stress distribution in all graft models after ATT at 0°, 30°, 60° and 90° can be seen in Figures 36-40. The contact pressure between the AM-AM and PL-PL bundles after ATT can be seen in Figure 41.

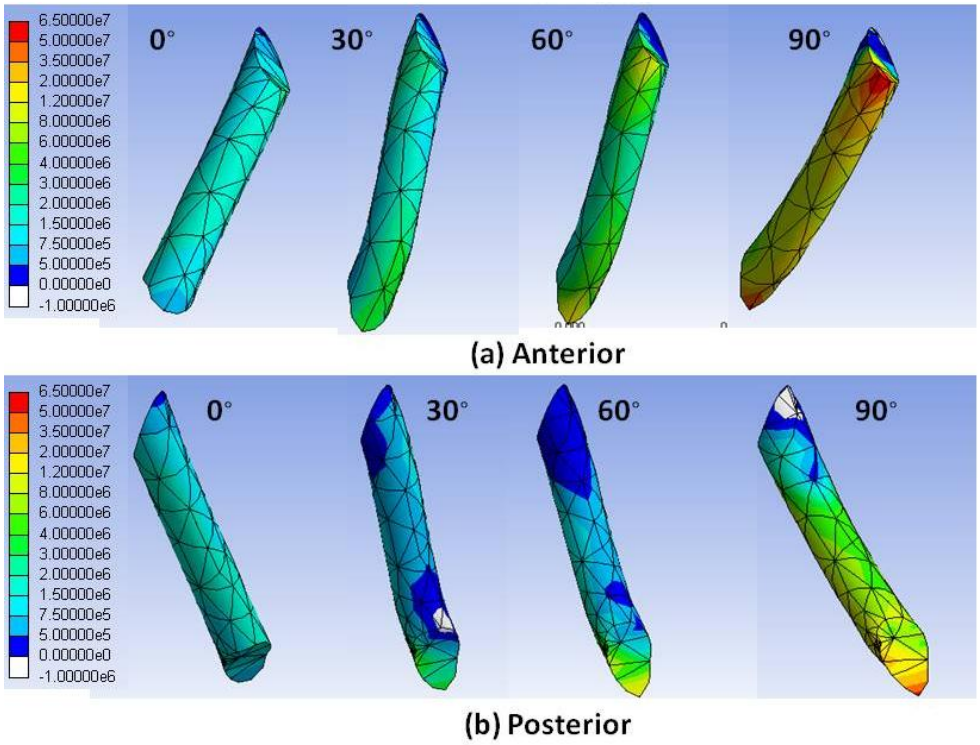

Figure 36: Stress in the AM-AM after ATT for stress-free initial condition

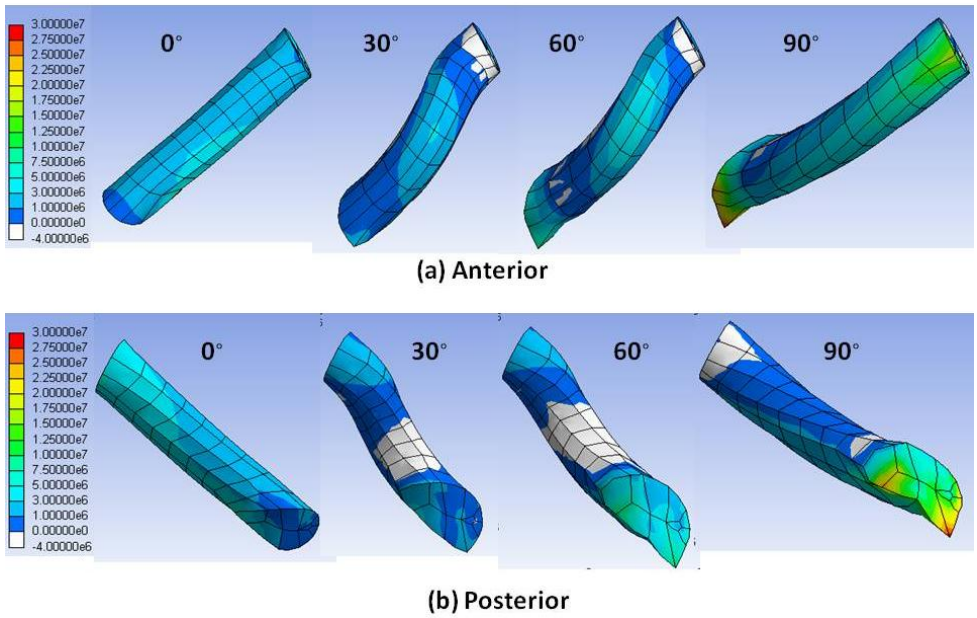

Figure 37: Stress in the PL-PL after ATT for stress-free initial condition

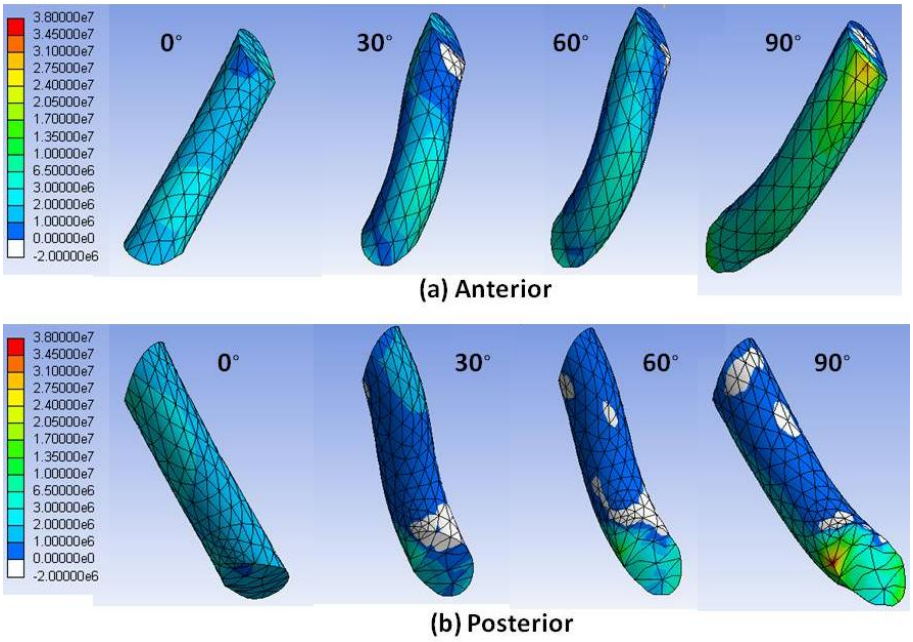

Figure 38: Stress in the Mid-Mid after ATT for stress-free initial condition

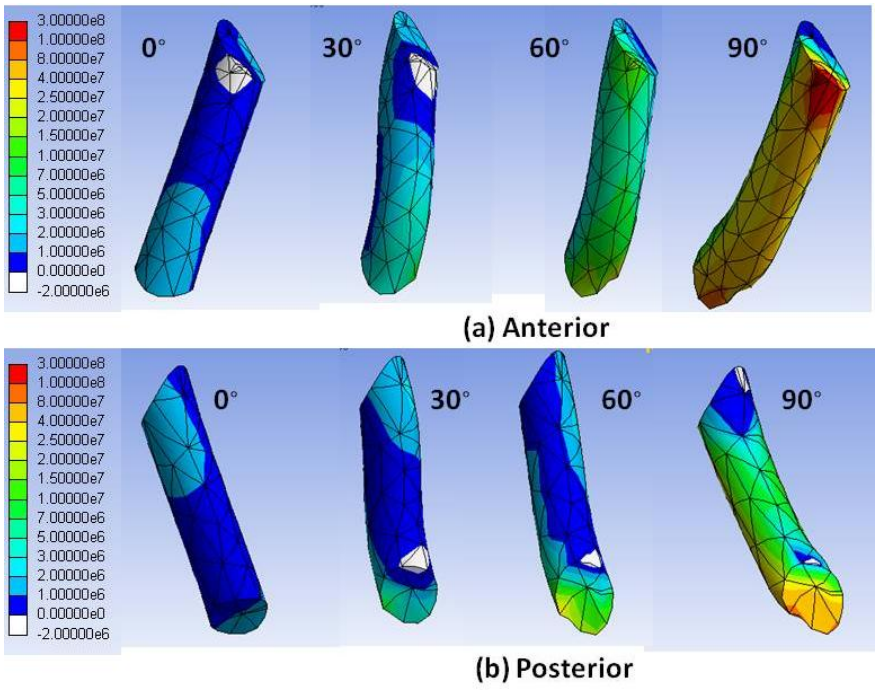

Figure 39: Stress in the PL-High AM after ATT for stress-free initial condition

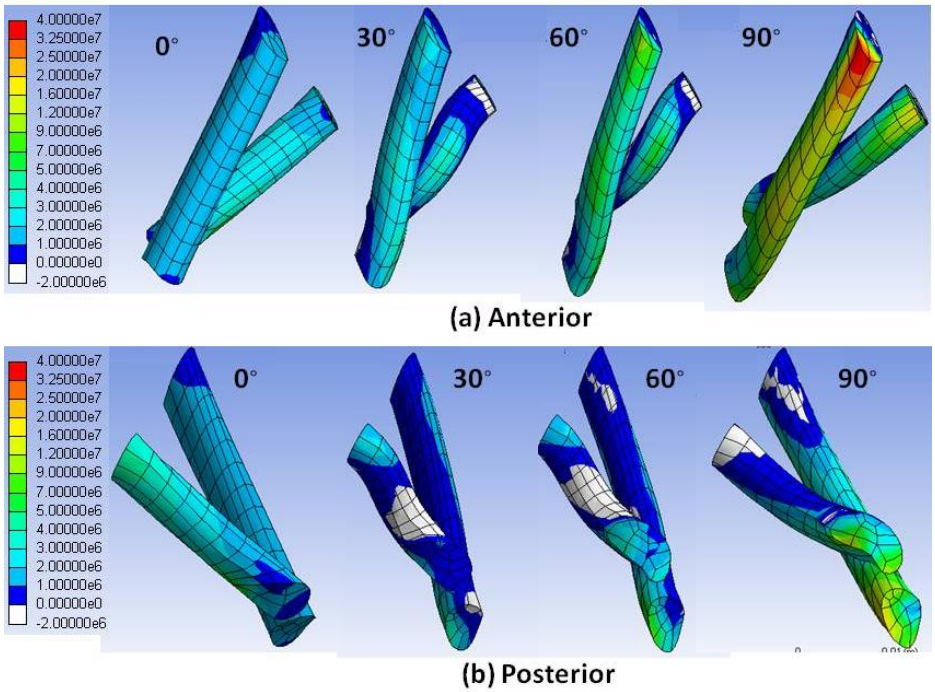

Figure 40: Stress in the DB after ATT for the stress-free initial condition

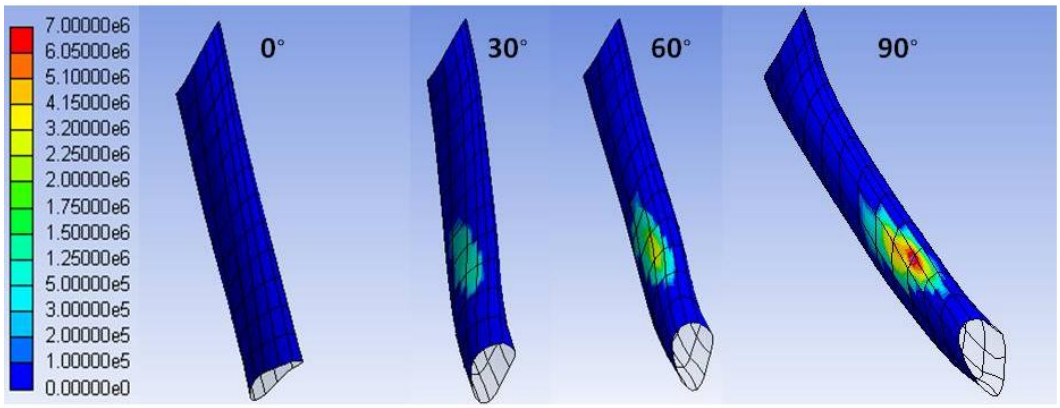

Figure 41: Contact pressure between AM-AM and PL-PL after ATT for stress-free initial condition

4.4.3 Pre-stress Initial Condition

The pre-stress initial condition was analyzed to determine the effect that a 40N initial tension had on graft behavior. The initial stress state was determined as previously described, and the results are summarized in the following section.

4.4.3.1 Graft Tension Figure 42 shows the tension in the grafts as a function of flexion angle for the pre-stressed state.

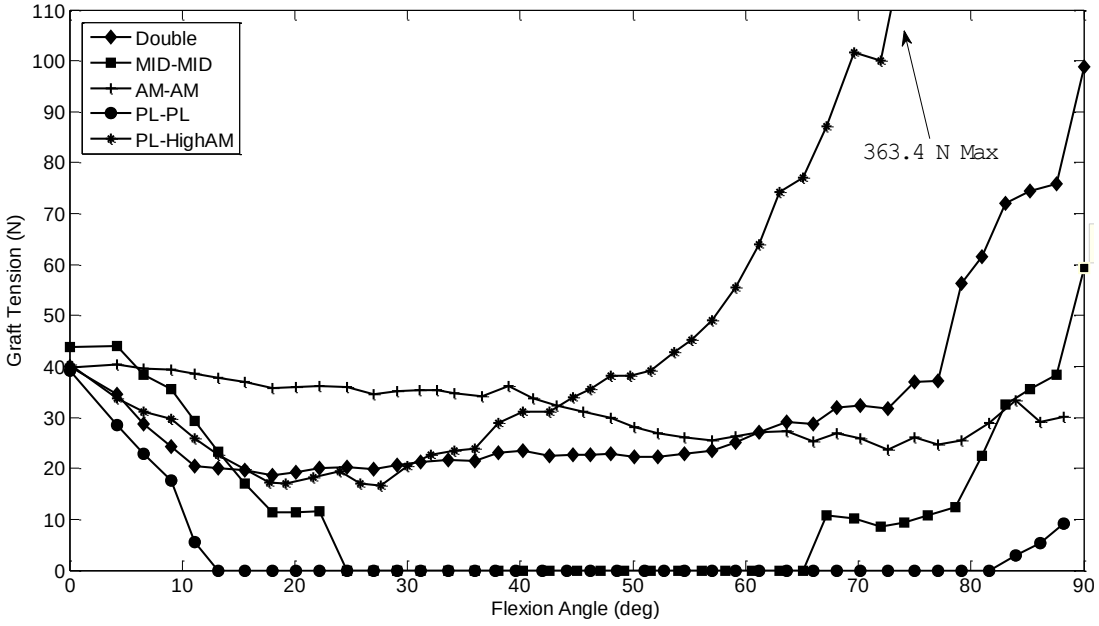

Figure 42: Graft tension vs. flexion angle for pre-stress initial condition

As seen in Figure 42, all graft models start with an initial tension of approximately 40 N at full extension. Initially, as flexion angle increases, the tension in all graft models decreases. The DB graft model decreases tension from 40N at 0° to a minimum of 28.7 N at 25° flexion and then steadily increases tension to a max value of 98.9 N at 90° flexion. The tension in the PL-High AM graft model decreases from 40N at 0° to minimum of 16.7N at 39° flexion and then dramatically increases to a maximum value of 363.4N at 90°. The tension in the PL-PL and Mid-Mid graft models steadily decreases from 40N to 0N at 12° and 24°, respectively. The PL-

PL graft model does not become taught again until 81°, where it steadily increases to a maximum value of 11.2N at 90°. The Mid-Mid graft model does not become taught until 63°, where it steadily increases to a max value of 59.3N at 90°. The tension in the AM-AM graft model remains relatively close to 40N, slowly decreasing to a minimum of 30.8 N at 90°. Figure 43 shows the tension in the graft models after application of the 89N anterior load (ATT) at flexion angles of 0°, 15°, 30° 45°, 60° and 90°.

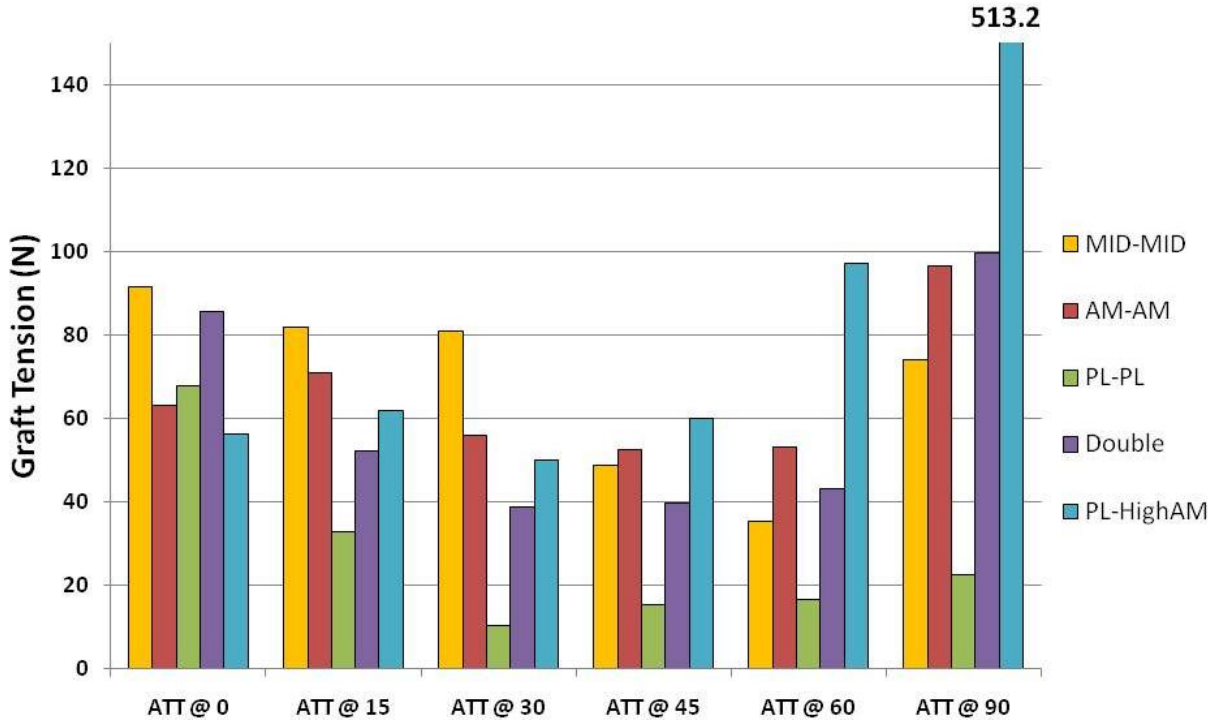

Figure 43: Graft tension after ATT for pre-stress initial condition

As seen in Figure 43, the graft tension in the PL-High AM model is the highest of all models at 90° flexion, with a maximum value of 513.2 N (partially excluded for clarity), approximately five times larger than any other graft model. At 0°, the graft tension after ATT in the Mid-Mid model is the highest at 91.6N and the PL-High AM is the lowest at 56.4 N. The PL-PL graft model has the lowest tension after ATT at flexion angles from 15°-90°.

4.4.3.2 Stress Analysis Figure 44 shows the peak stress (1st principal) as a function of flexion angle for the pre-stressed initial condition and Figure 45 shows the peak stress in the AM-AM and PL-PL graft models when treated as a single bundle (SB), and in combination as a double bundle (DB) model.

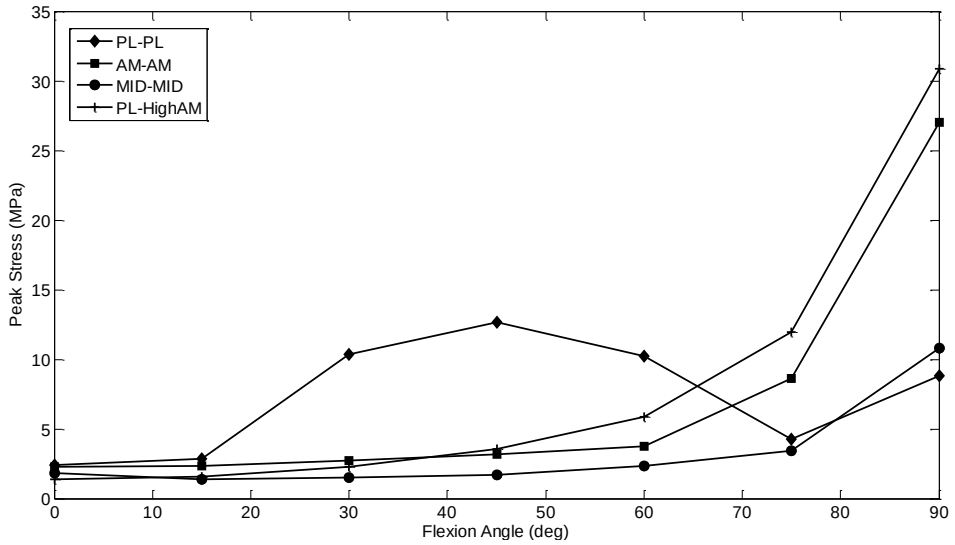

Figure 44: Peak stress vs. flexion angle in SB models for pre-stress initial condition

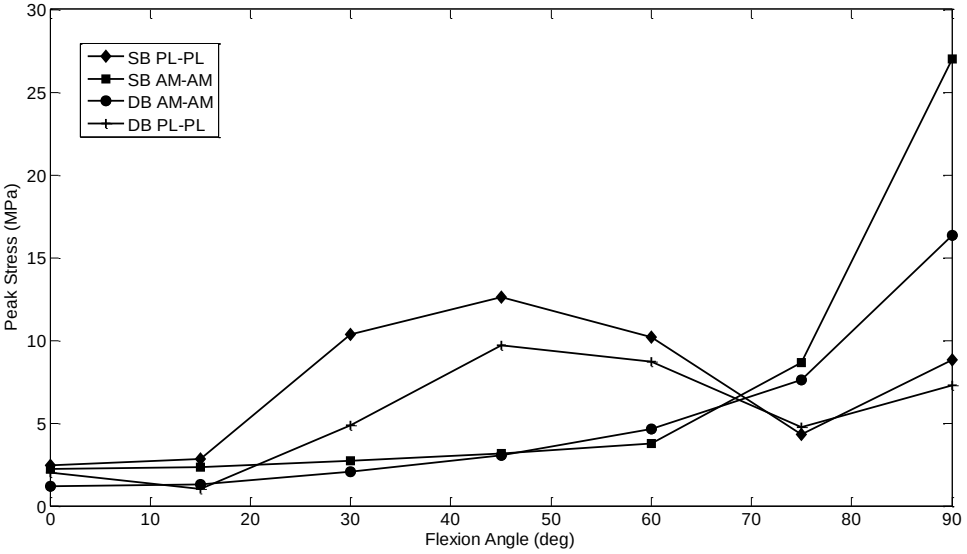

Figure 45: Peak stress vs. flexion angle for SB and DB AM-AM and PL-PL for pre-stress initial condition

As seen in Figure 44, the stress in the AM-AM and PL-High AM graft models follow similar trends, with a relatively constant peak stress until 60° flexion, then a dramatic increase to maximum values of 27.0 MPa and 30.8 MPa, respectively. The stress in the PL-PL graft model increases until 45° flexion to a maximum value of 12.6 MPa then decreases at a similar rate until 75° flexion and finally increases again at 90° flexion. The stress in the Mid-Mid graft model remains relatively constant until 75° flexion where it increases to a maximum value of 10.8 MPa at 90° flexion. As seen in Figure 45, when comparing the AM-AM and PL-PL graft models when treated as SB or DB, the peak stress in the DB PL-PL is less than that of the SB PL-PL at all flexion angles, except 75° when they are approximately equal. The maximum value occurs at 45° in both models, but decreases by 24% from 12.6 MPa to 9.6 MPa when modeled in combination as DB. The peak stress in the AM-AM graft is relatively unchanged when modeled solely or in combination, until 90°, where the peak stress decreases by 39% from 27.0 MPa to 16.3 MPa when modeled as DB. Figures 46-50 show the stress distribution in the graft models for the pre-stressed initial condition at flexion angles of 30°, 60° and 90°. Figure 51 shows the contact pressure between the AM-AM and PL-PL grafts in the DB graft model.

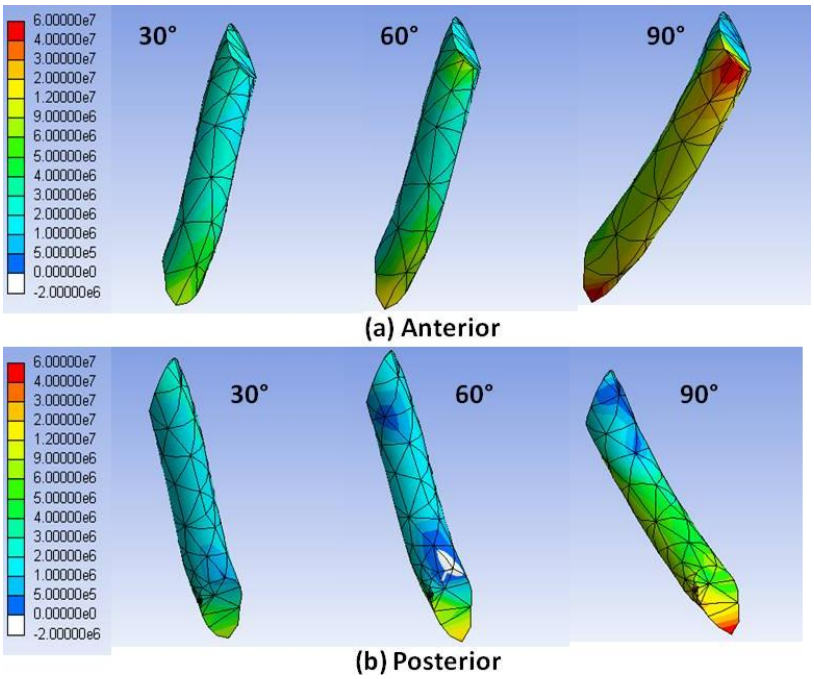

Figure 46: Stress in AM-AM during flexion for pre-stress initial condition

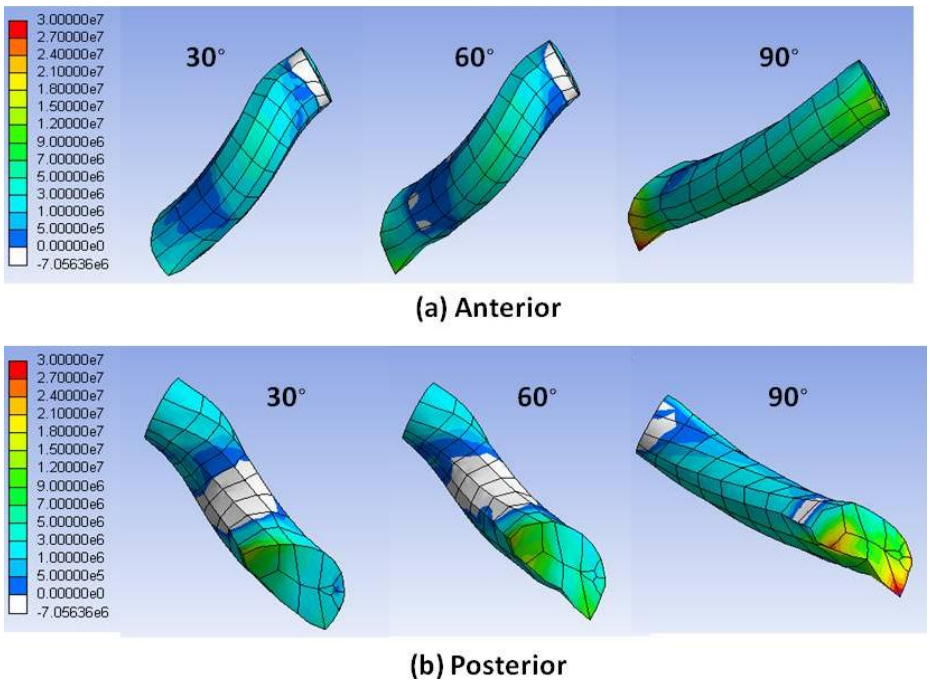

Figure 47: Stress in PL-PL during flexion for pre-stress initial condition

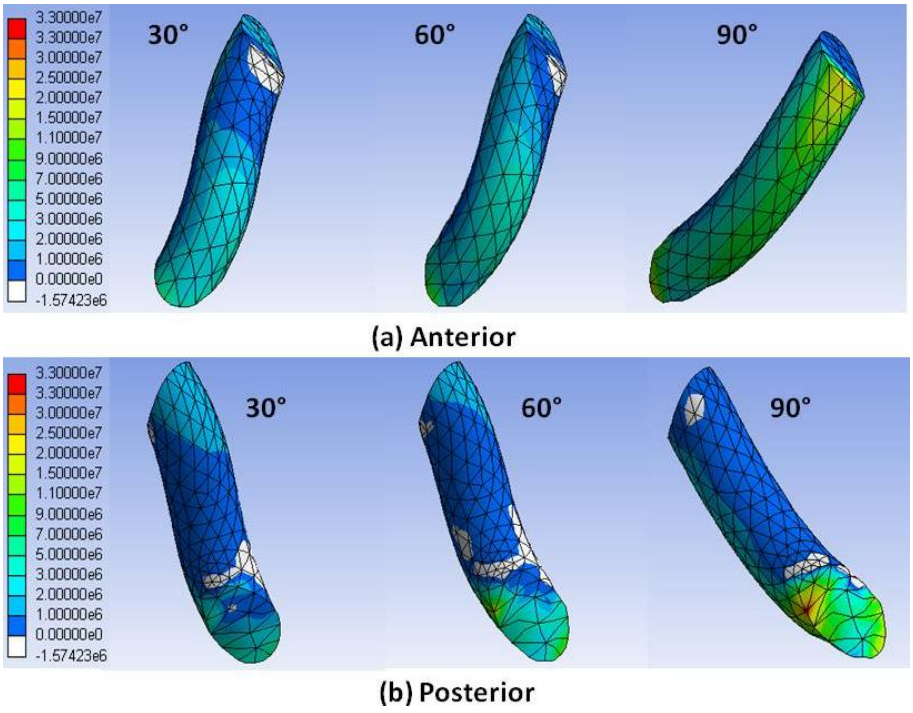

Figure 48: Stress in Mid-Mid during flexion for pre-stress initial condition

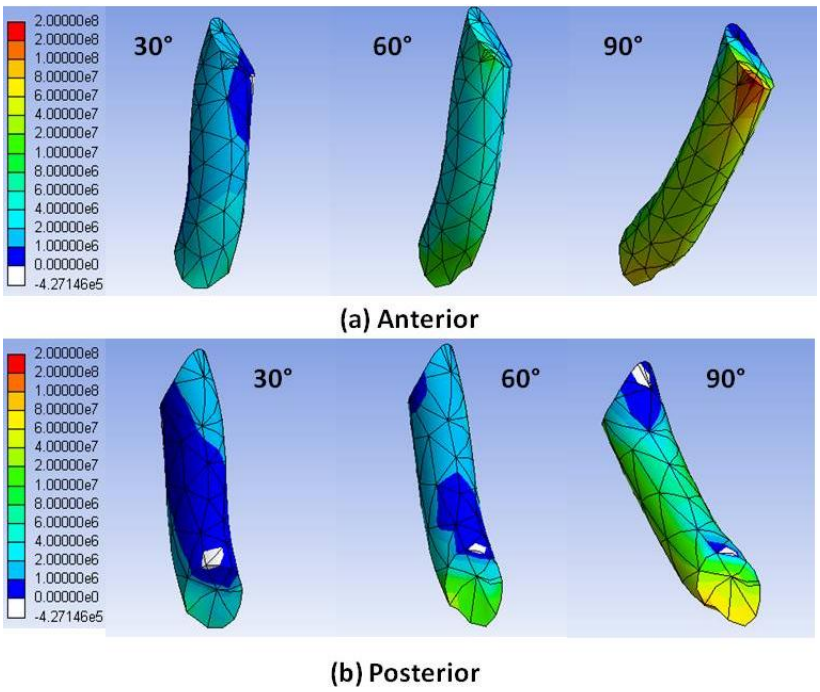

Figure 49: Stress in PL-High AM during flexion for pre-stress initial condition

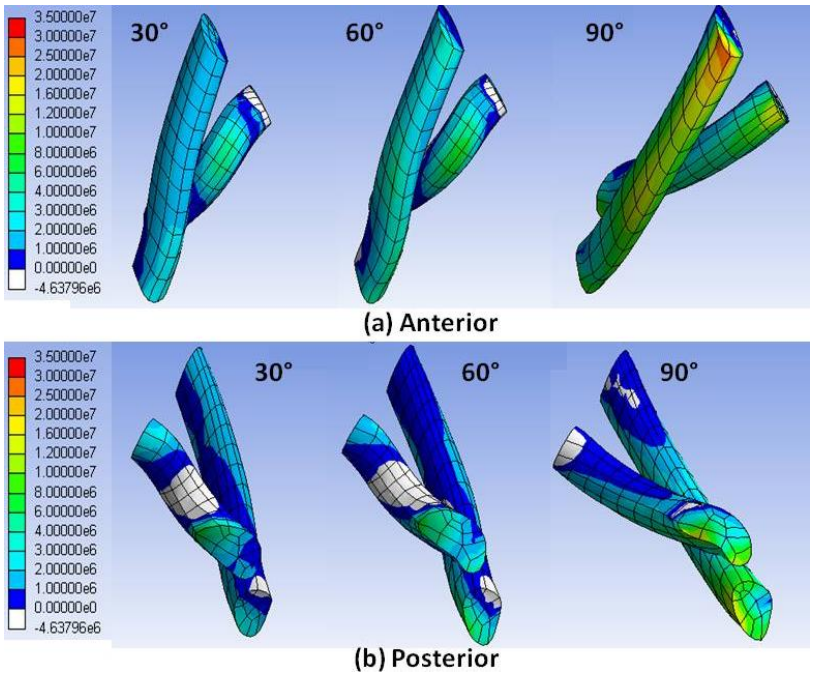

Figure 50: Stress in DB during flexion for pre-stress initial condition

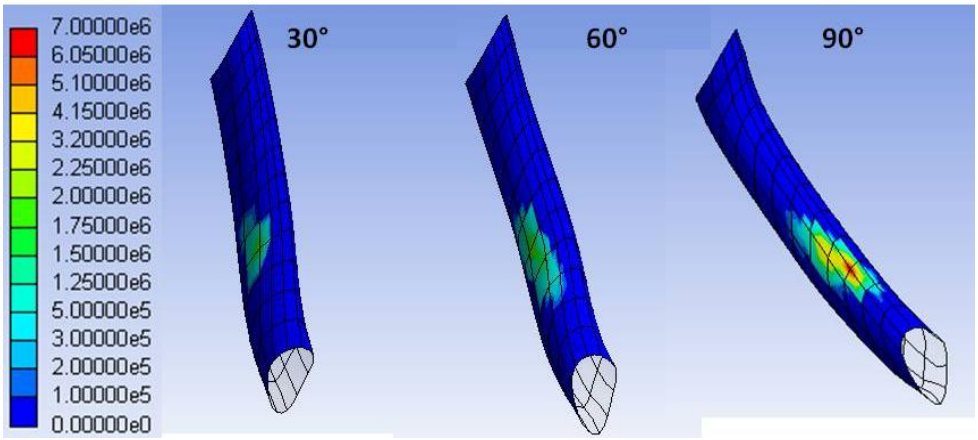

Figure 51: Contact pressure between AM-AM and PL-PL during flexion for pre-stress initial condition

Figure 52 shows the peak stress in all single bundle graft models after application of the 89N anterior tibial load (ATT) at all flexion angles for the pre-stress initial condition. Figures 53 and 54 show the peak stress in the AM-AM and PL-PL bundles when treated as SB and DB.

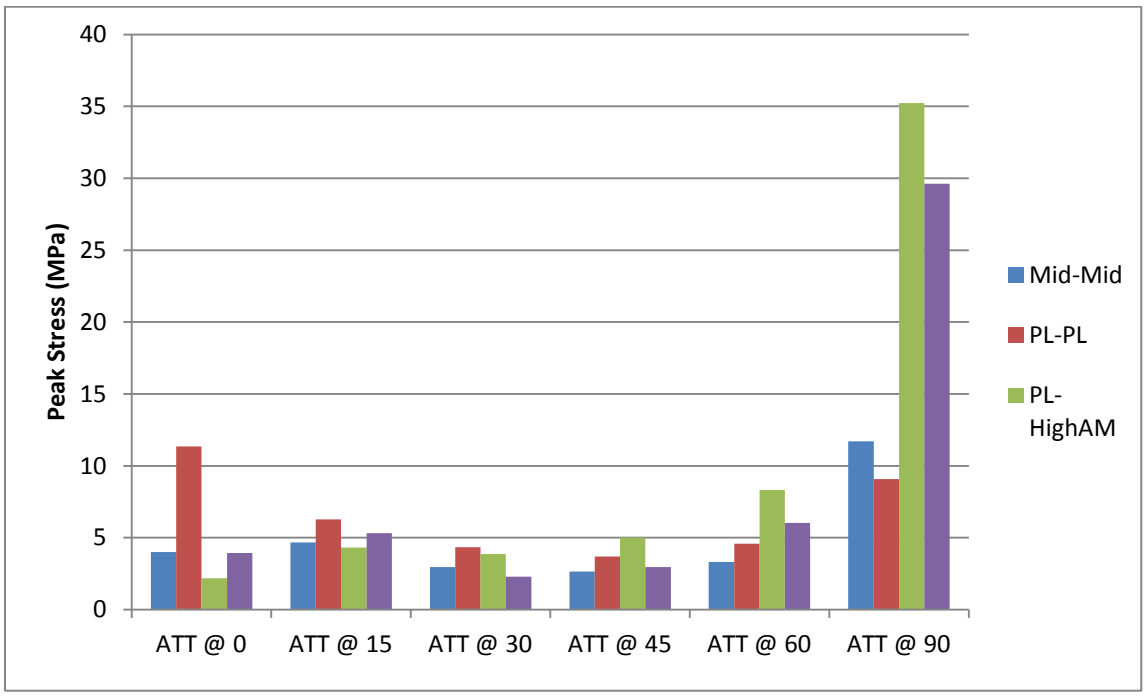

Figure 52: Peak stress in the SB models after ATT for pre-stress initial condition

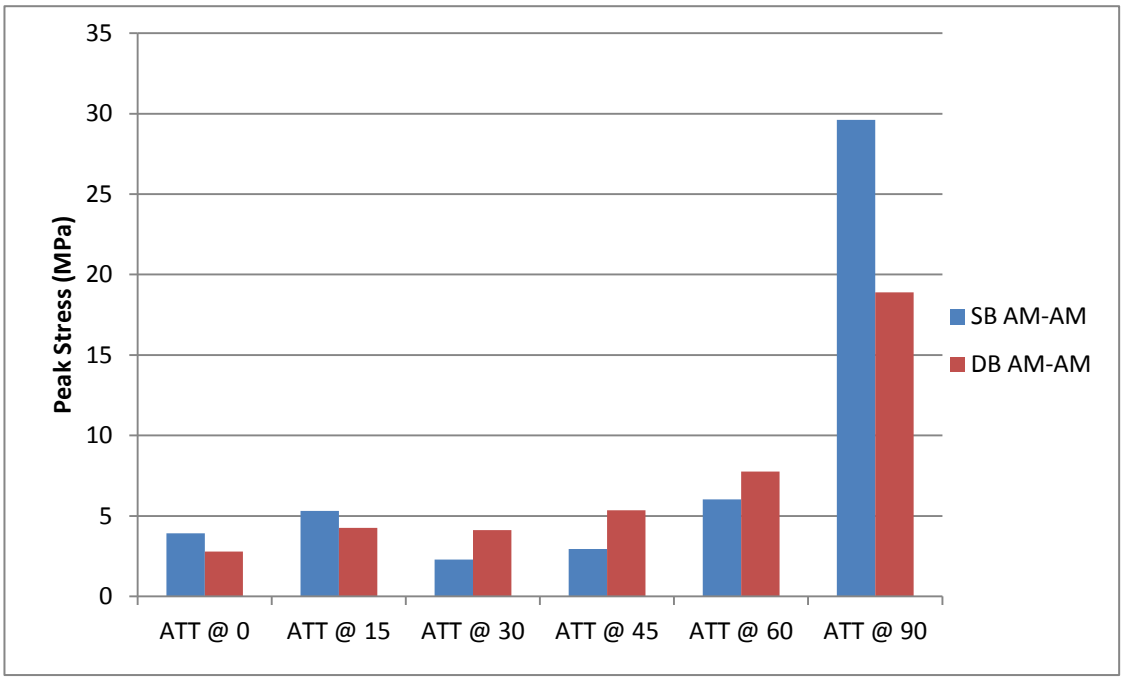

Figure 53: Peak stress in SB and DB AM-AM after ATT for pre-stress initial condition

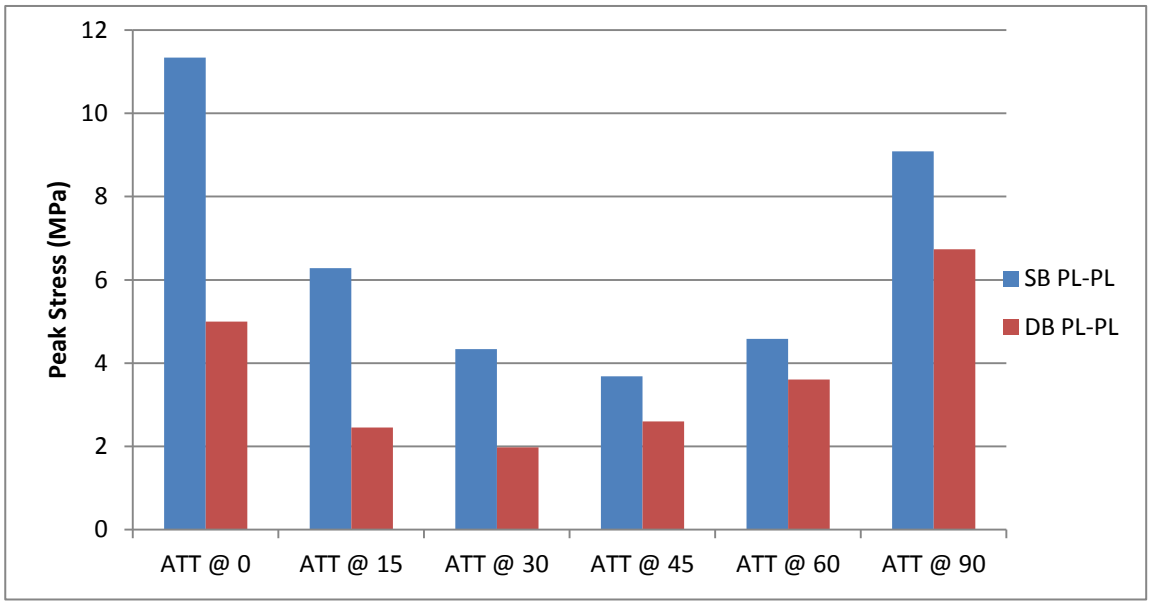

Figure 54: Peak stress in SB and DB PL-PL after ATT for pre-stress initial condition

As seen in Figure 52, the stress in the PL-PL graft model was the highest after ATT at 0°, with a peak value of 11.3 MPa, which is twice as high as any other graft model. The stress in the graft models after ATT at flexion angles of 15°, 30°, 45° were all relatively low, with peak values all below 6.3 MPa. After ATT at 60°, the PL – High AM graft model has a jump in peak stress to 8.4 MPa, while the peak stress in all other graft models remains below 6.3MPa. After ATT at 90° flexion, the peak stress in the PL-High AM and AM-AM graft models increases significantly to value of 35.2 MPa and 29.6 MPa, respectively. As seen in Figure 53, the peak stress in the SB AM-AM is greater than the DB AM-AM after ATT at 0°, 15° and 90° flexion with the largest difference at 90°, where the peak stress in the DB AM-AM is 36% less than the SB AM-AM, 18.8MPa compared to 29.6MPa. Conversely, the peak stress in the DB AM-AM is greater than the SB AM-AM after ATT at 30°, 45° and 60°, with the largest difference at 45°, where the peak stress in the DB AM-AM is 83% greater than the peak stress in the SB AM-AM, with values of 5.3 MPa and 2.9 MPa. As seen in Figure 54, the peak stress in the DB PL-PL graft is less than the SB PL-PL after ATT at all flexion angles. The largest difference is after ATT at 0°, where the peak stress in the DB PL-PL is more than half the peak stress in the SB PL-PL, with values of 5.0Mpa compared to 11.3 MPa. Figures 55-59 show the stress distribution in the graft models after ATT and Figure 60 shows the contact pressure between the AM-AM and PL-PL bundles in the DB model at flexion angles of 0°, 30°, 60° and 90° for the pre-stress initial condition.

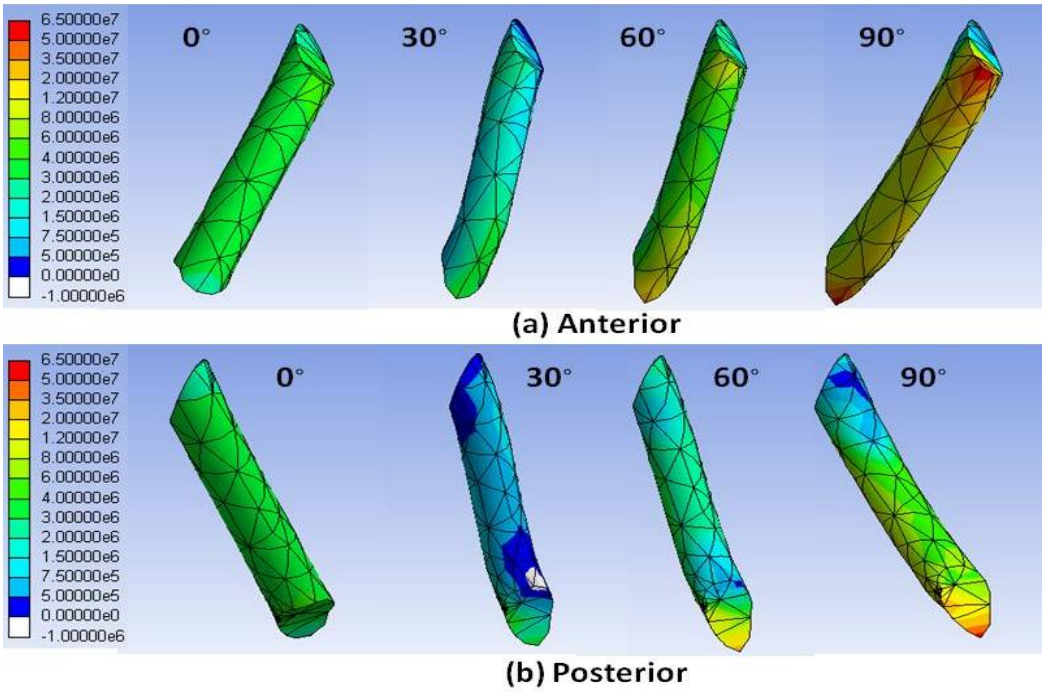

Figure 55: Stress in AM-AM after ATT for pre-stress initial condition

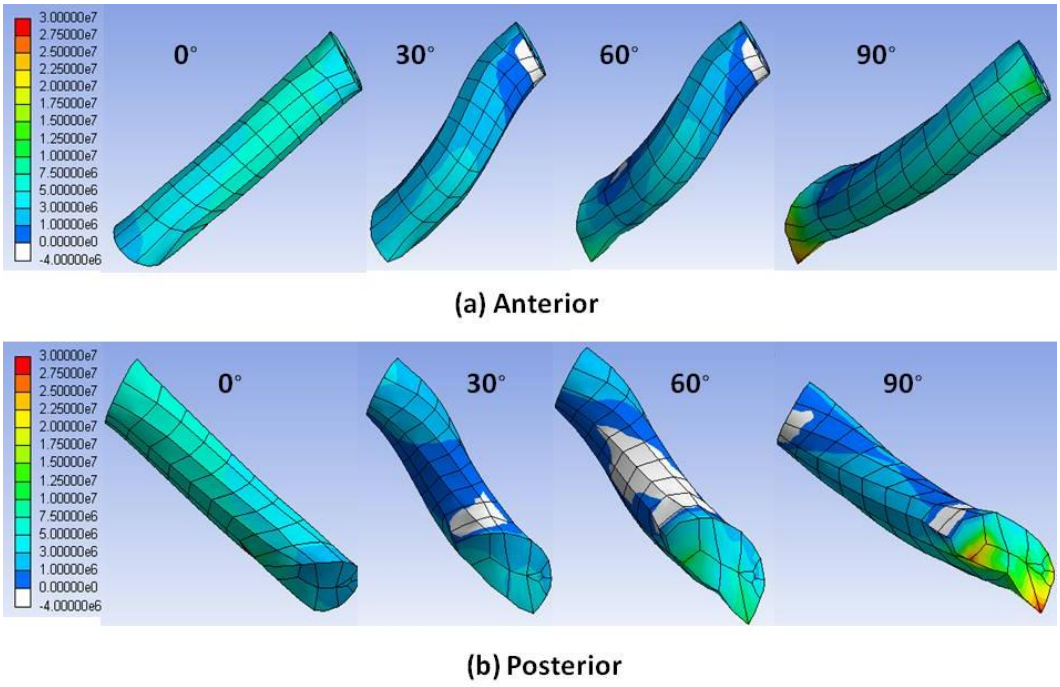

Figure 56: Stress in PL-PL after ATT for pre-stress initial condition

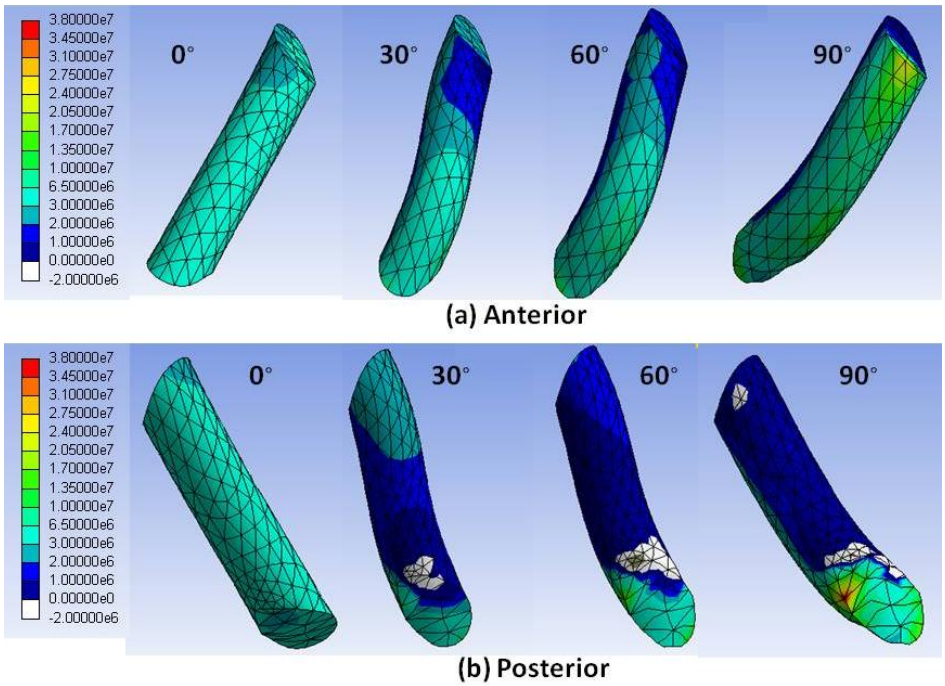

Figure 57: Stress in Mid-Mid after ATT for pre-stress initial condition

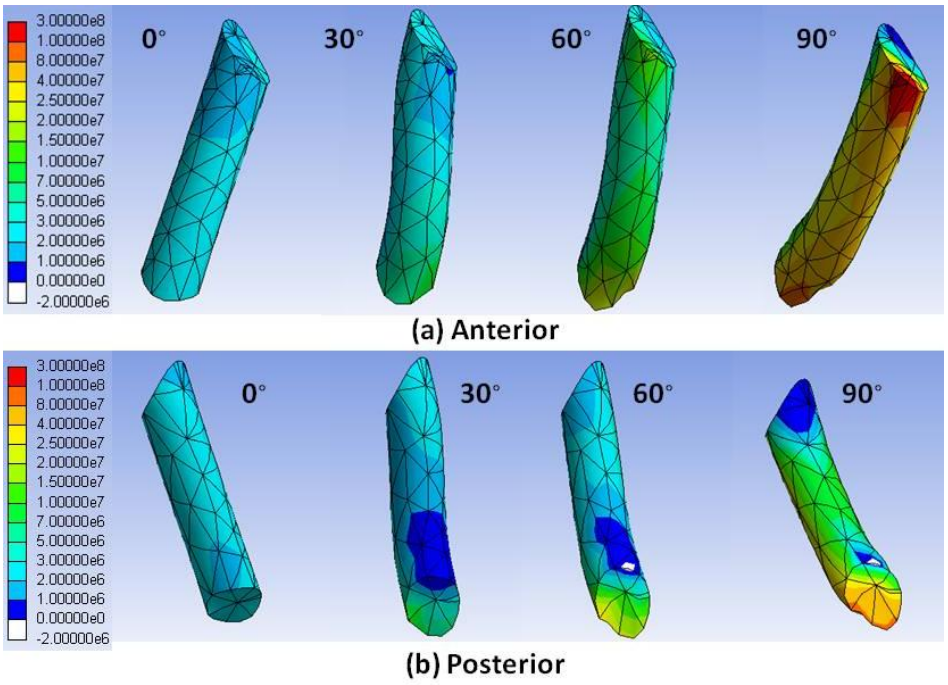

Figure 58: Stress in PL-High AM after ATT for pre-stress initial condition

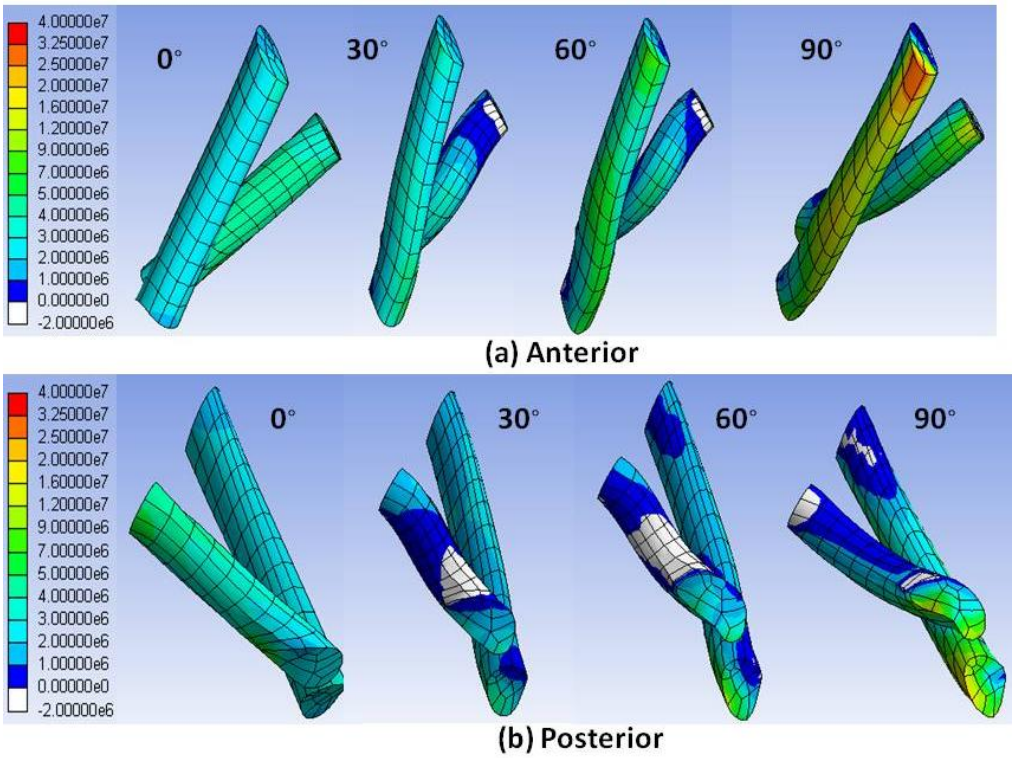

Figure 59: Stress in DB after ATT for pre-stress initial condition

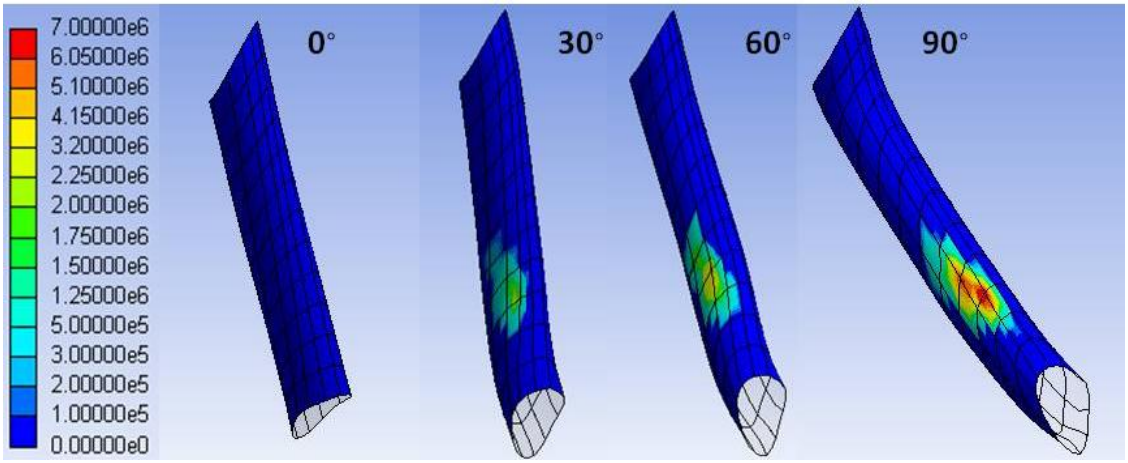

Figure 60: Contact pressure between AM-AM and PL-PL after ATT for pre-stress initial condition

4.5 DISCUSSION OF COMPUTATIONAL RESULTS

One goal of the computational analysis was to provide insight into which tunnel position provides the least amount of graft tension and stress when subject to passive flexion/extension and to determine the graft tensions and stresses after application of an 89N anterior tibial load at various flexion angles, since the primary function of the ACL is to resist anterior tibial translation. Another goal was to determine the effect that an initial stress from a 40N tension has on the graft behavior. In the following section, the results of the stress-free initial condition will be discussed for comparison across tunnel positions. The next section will discuss the results of the stressed vs. stress-free initial conditions.

4.5.1 Comparison of tunnel positions

4.5.1.1 Length Change Before any stress analysis, the distance between centers of the bone-graft interface (tunnel insertions) of each tunnel position as a function of flexion angle was determined. This provided insight into whether the graft models would be increasing or decreasing in length and hence in tension. The PL-PL model showed the most significant decrease in tunnel insertion length throughout flexion, which is consistent with previously published results (Yoo 2010, Kurosawa 1991). This decrease suggests that this graft model has minimal graft tension during flexion. The AM-AM graft model showed relatively no change in distance between tunnel sites, while the PL-High AM model steadily increased in length as a function of flexion angle. This suggests that the tension in the PL-High AM graft model may significantly increase as a function of flexion angle. It is important to note here that distance between the centers of tunnel insertions is not the only factor affecting graft tension. Off-center bending effects also create tensions in the graft. Since we are only looking at distance between *centers*, the effect of bending may be lost. This effect is discussed further the following subsection.

4.5.1.2 Graft Tension Graft tension was calculated from the reaction forces at the tibia-graft interface. The component of reaction force that was parallel to the long-axis of the graft was determined to be the graft tension. The first condition analyzed was the graft tension during flexion. Since this was a passive path, ideally the tension in the grafts would not have increased beyond an initial value, in this case 0 N. The DB, AM-AM, and PL-High AM all initiated tension earlier in the flexion path than the PL-PL and Mid-Mid graft models. This is consistent with the results from subsection 4.3.1 Change in Distance of Insertion Sites, where the PL-PL and Mid-Mid tunnel insertions had an overall decrease in length throughout flexion. However, as seen in Figures 22 and 23, at 90° flexion the change in distance between tunnel insertions of the Mid-Mid and PL-PL are still negative, but the graft tension is positive. This is most likely due to way tension was computed. When the graft undergoes high bending, the component of the reaction force parallel to the long axis may not adequately model tension. When a portion of the graft is bent, a component of the reaction force parallel to the long axis is in the shear direction. However, based on the current definition, this is falsely modeled as a tension and is therefore a major limitation. Since the PL-High AM had the greatest length change, it is no surprise that the tension in this graft is the highest, at an order of magnitude higher than any other graft model. This indicates that the PL-High AM graft model may not accurately reproduce the passive path that was found from robotic testing, and if this tunnel position is used, will most likely alter the natural path of flexion/extension.

The graft tension after ATT was the second condition for analysis. The primary function of the ACL is to resist ATT. A greater resistance to ATT would result in a higher graft tension after ATT. The DB graft model had the highest tension of all models after ATT at 0° flexion, and steadily decreased tension to 30°. This high tension at 0° is seen because the AM-AM and PL-PL are both taught, and are both contributing to resistance. The drop in tension after 0° is seen in the PL-PL model as well. This result is likely due to the decreasing length of the PL-PL graft. As the graft shortens, it will take more ATT to induce a tension. At flexion angles of 60° and 90° the PL-High AM graft model increases tension dramatically, compared to other models. This is mostly due to the already high stresses left on this graft model from flexion.

4.5.1.3 Stress Analysis The stress in the PL-PL graft model exhibited a different trend than all other graft models. The peak stress occurred at 45° while the peak stress in all other graft models occurred at 90°. This effect is due to the substantial shortening in the PL-PL model, causing the graft to buckle. This buckling produced a bending stress, which reached a maximum value at 45°. This is consistent with results from subsection 4.3.1 Change in distance of insertion sites, where the PL-PL model reached a maximum shortening at 45°. The stress distribution of the PL-PL graft model better illustrates this effect. There is tensile stress on the anterior side and compressive stress (white regions) on the posterior side at flexion angles of 30° and 60°. The stress in the PL-High AM and AM-AM showed similar trends consistent with a steady length increase. The shape of this curve is consistent with a uni-axial stress-displacement curve of the ACL (Xie 2009). The Mid-Mid graft had a relatively slow increase in stress as a function of flexion angle. It is important to note here that the stress values reported are taken at nodes in the middle 80% of the graft length. The peak stresses in all graft models occurred at the bone-graft interface, which can be seen in the stress distribution contour plots. However, this interface cannot be adequately modeled due to lack of physiologic graft geometry and little knowledge of the contact mechanism between bone and healing graft. This is a possible reason why the peak stress in the PL-High AM model is not significantly higher than other graft models, as seen with graft tension.

Since the DB model was a combination of the PL-PL and AM-AM graft models, each bundle was analyzed separately for stress. Generally, the peak stress during flexion in the PL-PL and AM-AM graft was less when modeled in combination compared to when modeled solely. The two bundles initially come in contact with each other at 11° flexion, resulting in a contact pressure which can be seen in Figure 37. The contact pressure reached a maximum value of 6.89 MPa at 90° flexion. Since the input to the model was displacement, prior to coming in contact, the stress in each respective bundle should be equivalent to the stress in the AM-AM and PL-PL models. This is true for the AM-AM bundle, however the PL-PL bundle had a slightly lower peak stress when modeled in combination prior to coming in contact. This difference is unexpected and is most likely due to a computational artifact arising from the additional contact pair in the DB model. The reduced stress in the PL-PL and AM-AM bundles when modeled in combination suggests that the contact between the two bundles acts to reduce the overall peak stress in each bundle during flexion.

The next condition for analysis was the peak stress after ATT. The PL-PL model had the highest stress after ATT at 0° flexion, which was an unexpected result considering it did not have the highest tension during this motion. ATT after flexion angles of 15°, 30°, 45° and 60° show that all graft models have a peak stress at or below 7MPa. At 90°, the PL-High AM and AM-AM showed the highest peak stress. This is due to the already high stress left on the model from flexion. Figures 25 and 26 show the peak stress in the AM-AM and PL-PL after ATT when they are modeled solely (SB) and in combination (DB). The AM-AM graft did not have much difference at 0° and 15°. However, after contact, at 30°, 45° and 60° the DB AM-AM graft model had greater stress after ATT than the SB AM-AM model. This is result is different than what was seen in flexion, when the DB model had reduced stress at all flexion angles after contact. This similar trend can be seen in the PL-PL, although, the DB PL-PL does not have a greater stress than the SB PL-PL until 45°. Both the DB PL-PL and DB AM-AM had significantly less peak stress than the SB models at 90°. These results suggest that the contact between the AM-AM and PL-PL bundles plays a significant, but different, role in the peak stress during flexion and after ATT.

4.5.2 Stressed vs. stress-free initial condition

The second goal of this study was to determine the effect that a pre-stress, resulting from a 40N initial tension, had on graft behavior. The 40N initial tension was chosen because this is a common initial tension applied to replacement grafts in ACL reconstruction. The results from each tunnel position can be seen in subsection 4.3.3 Pre-stress Initial Condition. In the following section, the results from the zero stress and pre-stress initial conditions will be compared.

4.5.2.1 Graft Tension In all graft models the tension decreased from the initial amount at the start of flexion. In the pre-stress state the AM-AM graft model decreased tension, from the initial 40N at 0° to 28.7N at full flexion, which was less than the tension in the zero stress case of 30.1N. Conversely, the tension in the DB graft model was nearly five times higher after flexion in the pre-stressed state. Since the tension in the PL-PL graft model remained nearly unchanged beyond the initial drop in tension, this result is surprising and is due to the definition of tension.

Although the tension in the PL-PL model did not change beyond the initial decrease, the overall reaction force changed and since the DB reaction force was the sum of the PL-PL and AM-AM reaction forces, this effected the DB tension. The Mid-Mid graft model had considerably higher tension at full flexion in the pre-stress state.

After ATT at 0°, 15° and 30° the Mid-Mid graft model had the highest tension of all models in the pre-stressed state, and was considerably higher than the zero stress state. Interestingly, all graft models displayed higher tensions after ATT in the pre-stressed state except for the PL-PL graft model, which remained relatively unchanged at 30 and 60°. This is most likely because the PL-PL graft model is never fully taught during flexion, and a zero tension is observed at 30° and 60°, regardless of a stressed or stress-free initial condition.

4.5.2.2 Stress Analysis The peak stress in all single bundle graft models remained relatively unchanged between the pre-stress and stress free states except at low flexion angles, where the pre-stress caused a higher peak stress. Perhaps the most interesting result was with the DB model during flexion. Specifically, the pre-stressed DB PL-PL bundle had considerably less peak stress than the stress free DB PL-PL during flexion. This is likely because in the pre-stressed state, the PL-PL to remain taught longer, and therefore did not bend as much as in the stress free state, and therefore had a lower peak stress. Also, the contact pressure between the AM-AM and PL-PL bundles during flexion is greater in the pre-stress state, which may have attributed to the difference in stress.

During ATT, the peak stress in all single bundle models remained relatively unchanged between the pre-stress and stress free state except at 0°, where the stress in the PL-PL model nearly doubled in the pre-stress state. In the DB model, the peak stress after ATT in the PL-PL bundle was significantly less and the peak stress in the AM-AM bundle was greater in the pre-stressed state. This indicates that the AM-AM bundle has a greater role to resist ATT when a pre-stress is applied to both bundles. This change in peak stress can be seen when comparing the stress distributions after ATT in the DB model, for both initial conditions.

There were some limitations in the current model. The boundary conditions at the graft-bone interface were treated as bonded; however, this is not the case clinically. Prior to healing, the graft is fed through the bone tunnels and secured rigidly on the outer surface of each bone. The complex interaction between the graft and bone is difficult to model as this would include

unknown frictional parameters that would affect the overall stress distribution. The material model used for the graft was isotropic; however ligaments and tendon are anisotropic due to the composite like structure of the collagen fibers embedded in a proteoglycan matrix. One theory is that the collagen fibers do not support compressive loads. Another major limitation was the way tension was calculated. The tension was the component of reaction force that was parallel to the long axis of the graft. This is acceptable for a graft that is straight, as the normal force would be in the direction of the long-axis. However, when the graft bends, the normal throughout the graft changes, and therefore the tension is not constant. This is seen in the PL-PL model, which has the most significant amount of bending. The length of the graft decreases, although there is still a tension. This is because there is a shear component, which was inaccurately modeled as a tension. Finally, the kinematics used were for the intact knee, and it is unknown whether the kinematics of the knee would change after a reconstruction. However, one goal of ACL reconstruction is to reproduce the intact kinematics, therefore, by using intact kinematics one can determine whether a certain reconstruction is suitable. For instance, the tension in the PL-High AM model was very high during passive flexion/extension, where ideally the tension would be zero. This is an indication that this model may be insufficient in reproducing the passive path of the intact knee.

5.0 COMPUTATIONAL VS. EXPERIMENTAL

For experimental comparison, the in-situ force after ATT at 0°, 15°, 30°, 60° and 90° can be compared to model predictions of graft tension after ATT at these flexion angles. Figure 61 shows the in-situ force in each graft determined experimentally and the model predictions for a stress-free (zero tension) and pre-stress (40 N initial tension) initial condition.

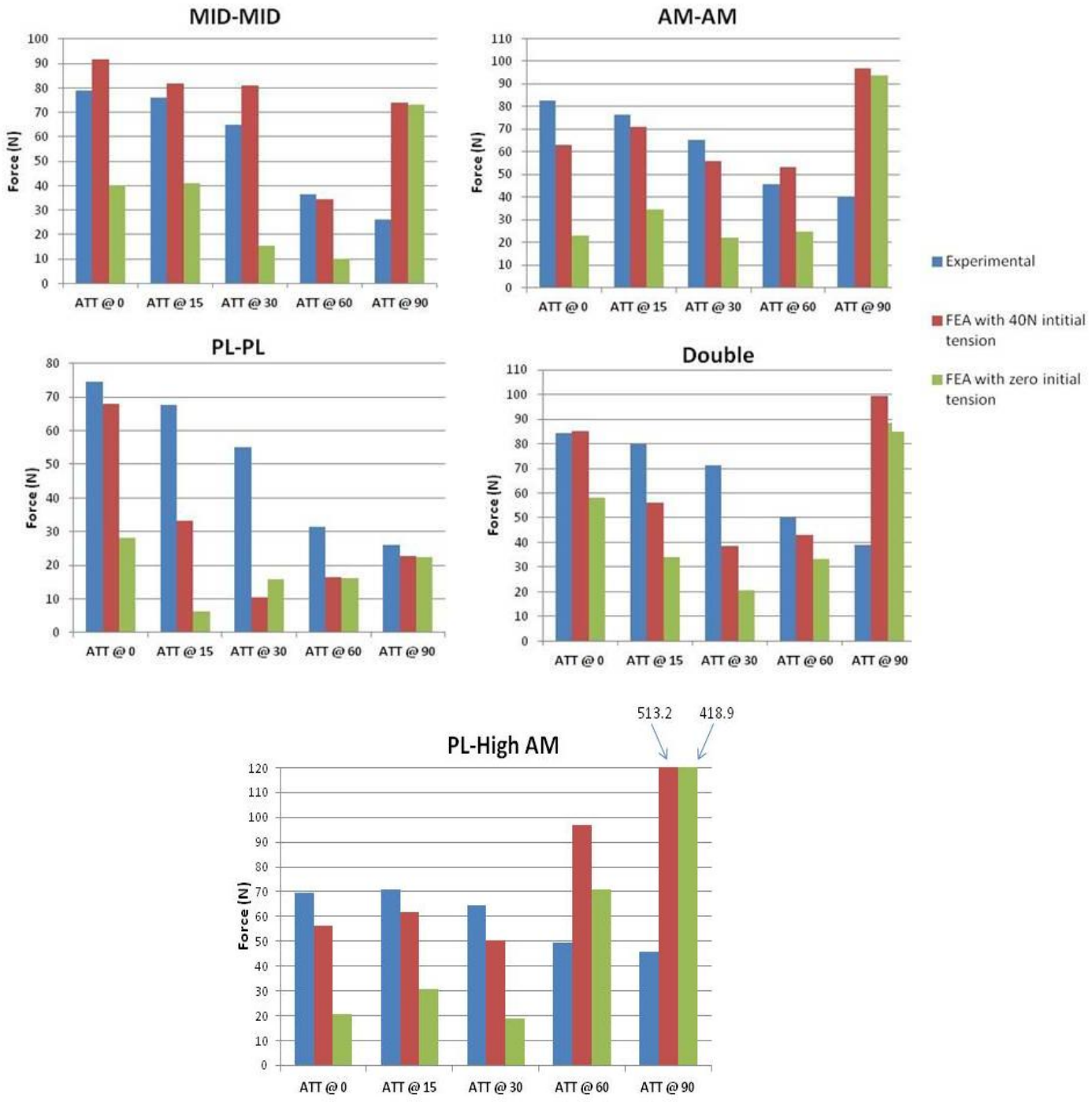

Figure 61: Experimental and computational graft force after ATT

As seen in Figure 61, all graft models except the PL-PL were closer to experimental values after ATT at flexion angles of 0°, 15°, 30° when they were given an initial tension of 40N compared to no initial tension. The Mid-Mid graft model overestimated the graft force with a 40N initial tension, while all other graft models tended to underestimate the experimental graft forces. In all cases except the PL-PL model, the difference between model and experimental was greatest after ATT at 90°. The graft tension in Mid-Mid and AM-AM models with 40N initial tension were the closest to experimental values at all flexion angles except 90°, while the PL-PL model closely matched the experimental values at 90°.

6.0 CONCLUSIONS

From the comparison of experimental vs. computational, overall the graft forces in the 40N initial tension case more closely matched experimental values. This result was expected considering the experimental tests protocol included an application of 40N tension at a 30° flexion angle, thus providing a measure of validation for the computational model. The PL-High AM graft model produced very high non-physiologic forces when subject to the intact passive path of flexion. This indicates the PL-High AM reconstruction may be unable to reproduce the intact kinematics.

There were limitations in the current model, which were discussed previously. To overcome these limitations, the following future work is proposed. The boundary conditions on the graft-bone interface were treated as bonded. A more realistic approach would be to model the graft by inserting it into the bone tunnels and securing it rigidly on the outer surface of the bone, which is done clinically. However, this would be difficult because frictional parameters between the graft and bone tunnel are difficult to model. Another limitation was the assumption of isotropy. In future work, one could model the ligament as a transversely isotropic composite like structure. To include this anisotropy in the FE model, one could combine two separate strain energy functions for the fiber and matrix. The matrix would be isotropic but the fibers would have a local material coordinate system applied to the long axis where directionally dependent material properties could be assigned. Perhaps the most significant limitation was the way tension was calculated. A more accurate way to calculate tension may be to take slices along the length of the graft and compute the average normal force for each slice. Then one could either average them across all slices, for an overall tension, or focus on a point of interest, such as the middle. Finally, knee kinematics for each reconstruction could be determined experimentally. These may or may not be similar to intact. Therefore, for more accurate results, each reconstruction would have its own kinematics, instead of using the intact kinematics for all cases.

BIBLIOGRAPHY

Bedi A, Altchek D. The "Footprint" Anterior Cruciate Ligament Technique: An Anatomic Approach to ACL Reconstruction. *Arthroscopy: The Journal of Arthroscopy and Related Surgery.* 2009; 25,10: 1128-1138

Chhabra A, Starman J, Ferretti M, Vidal A, Zantop T, Fu F. Anatomic, Radiographic, Biomechanical and Kinematic Evaluation of the Anterior Cruciate Ligament and its Two Functional Bundles. *Journal of Bone and Joint Surgery.* 2006; 88-A: 2-10

Cohen S, Fu FH. Three portal technique for Anterior Cruciate Ligament Reconstruction: Use of a Central Medial Port. *Arthroscopy: The Journal of Arthroscopy and Related Surgery.* Vol 23 No.3: 2007: 325e1 – 325e4.

Comninou M, Yannas IV. Dependence of Stress-Strain Non-linearity of Connective Tissue on the Geometry of Collagen Fibers. *Journal of Biomechanics.* 1976; vol. 9: 427-33

Danto M, Woo SL. The Mechanical Properties of Skeletally Mature Rabbit Anterior Cruciate Ligament and Patellar Tendon Over a Range of Strain Rates. *Journal of Orthopaedic Research.* 1993 (11); 58-67.

Darcy SP, Kilge RHP, Woo SL-Y, Debski R. Estimation of ACL Forces by Reproducing Knee Kinematics between Sets of Knees: A Novel Non-invasive Methodology. *Journal of Biomechanics.* 2006; 39: 2371-2377

Dayal N, Chang A, Dunlop D, Hayes K, Chang R, Cahue S, Song J, Torres L, Sharma L. The Natural History of Anteroposterior Laxity and its Role in Knee Osteoarthritis Progression. *Arthritis and Rheumatism.* Aug 2005 Vol. 52; 8. pp 2343-2349.

Duenwald S, Vanderby R, Lakes RS. Constituitive Equations for Ligament and Other Soft Tissue: Evaluation by Experiment. *Acta Mechanica*. 2009; 205: 23-33

Fisher KJ, Manson TT, Pfaeffle HJ, Tomaino MM, Woo SL-Y. A Method for Measuring Joint Kinematics Designed for Accurate Registration of Kinematic Data to Models Constructed from CT Data. *Journal of Biomechanics.* 34 (2001) 337-383.

Fujie H, Mabuchi K, Woo SLY, Livesay GA, Avai S, Tsukamoto Y. The Use of Robotic Technology to Study Human Joint Kinematics: A New Methodology. *Journal of Biomechanical Engineering.* 1993. Vol. 115; 211-217.

Gilbertson LG, Doehring TC, Kang J. New Methods to Study Lumbar Spine Biomechanics: Delineation of In-vitro Load Displacement Characteristics by Using a Robotic/UFS Testing System with Hybrid Control. *Operative Techniques in Orthopaedics.* October 2000; vol. 10(4): 246-253

Holzapfel G A, Non-linear Solid Mechanics: A Continuum Approach for Engineering. John Wiley and Sons. 2000.

Kato Y, Ingham SJ, Kramer S, Smolinski P, Saito A, Fu FH. Effect of Tunnel Position for Anatomic Single Bundle ACL Reconstruction on Knee Biomechanics in a Porcine Model. *Knee Surg and Sports Traumatol and Arthrosc.* (2010); 18: 2-10

Kurosawa H, Yamakoshi K, Yasuda K, Sasak T. Simultaneous measurement of changes in length of the cruciate ligaments during motion. *Clincal Orthopeadics and Related Research.* Apr. 1991; (265): 233-40.

Li RT, Lorenz S, Xu Y. Harner CD, Fu FH, Irrgang JJ. Predictors of Radiographic Knee Osteoarthritis After Anterior Cruciate Ligament Reconstruction. *American Journal of Sports Medicine.* Oct 21 2011. E-pub ahead of print.

Limbert G, Taylor M, Middleton J. Three Dimensional Finite Element Modeling of the Human ACL: Simulation of Passive Knee Flexion with a Stressed and Stress-free ACL. *Journal of Biomechanics* vol. 37 (2004) 1723-1731.

Lyman S, Koulouvaris P, Sherman S, Do H, Mandl L, Marx R. Epidemiology of Anterior Cruciate Ligament Reconstruction: Trends, Readmissions and Subsequent Knee Surgery. *Journal of Bone and Joint Surgery.* 2009; 91:2321-8

Martin B, Burr D, Sharkey N. *Skeletal Tissue Mechanics.* Springer-Verlag. New York. 1998.

Pena E, Martinez MA, Calvo B, Palanca D, Doblare M, A finite Element Simulation of the Effect of Graft Stiffness and Graft Tensioning in ACL Reconstruction. *Clinical Biomechanics* 20 (2005) 636-644

Pena E. Calvo B. Martinez M. Doblare M. An Anisotropic Visco-hyperelastic Model for Ligaments at Finite Strains. Formulation and Computational Aspects. *International Journal of Solids and Structures.* 44. (2007). Pp 760-778.

Pioletti, DP, Rakotomanana, LR, Benvenuti, JF, Leyvraz PF. Viscoelastic Constitutive Law in Large Deformations: Application to human knee ligaments and tendons. *Journal of Biomechanics.* 31 1998, 753-757.

Rudy TW, Livesay GA, Woo SL-Y, Fu FH. A Combined Robotic/Universal Force Sensor Approach to Determine In-situ Forces of Knee Ligaments. *Journal of Biomechanics.*1996. vol.29(10):1357-1360

Snow M, Campbell G, Addington J, Stannish WD. Two to five year result of primary ACL reconstruction using double tibialis autograft. *Knee Surg. Sports. Traumatol. Arthrosc.* Oct. 2010; 18(10) 1374-8

Song Y, Debski R, Musahl V, Thomas M, Woo S L-Y. A Three Dimensional Finite Element Model of the Human Anterior Cruciate Ligament: A Computational Analysis with Experimental Validation. *Journal of Biomechanics.* 37 (2004) 383-390.

Veronda, D.R., Westmann, RA., Mechanical Characterization of skin-finite deformations. *Journal of Biomechanics.* 3 (1970) 111-124.

Weiss J, Gardiner J. Computational Modeling of Ligament Mechanics. *Critical Reviews in Biomedical Engineering.* 29(4): 1-70. 2001.

Weiss JA, Gardiner JC, Ellis BJ, Lujan TJ, Phatak NS. Three-dimensional Finite Element Modeling of Ligaments: Technical aspects. *Medical Engineering and Physics.* 27 (2005) 845-861.

Weiss JA, Maker BM, Govindjee S. Finite Element Implementation of Incompressible, Transversely Isotropic Hyperelasticity. *Comput. Meth. Appl. Mech. Engrg.* 135(1996); 107-128

Wu C, Noorani S, Vercillo F, Woo S L. Tension Patterns of the Anteriomedial and Posterolateral grafts in a Double-Bundle Anterior Cruciate Ligament Reconstruction. *Journal of Orthopaedic Research.* 2009; 27: 879-884

Xie F, Yang L, Guo L, Wang Z-J, Dai G. A study on construction three-dimensional non-linear finite element model and stress distribution analysis of anterior cruciate ligament. *Journal of Biomechanical Engineering.* Dec 2009; vol. 131. 1-6

Yoo YS, Jeong WS, Shelty NS, Ingham SJ, Smolinski P, Fu F. Changes in ACL length at different knee flexion angles: an in-vivo biomechanical study. *Knee Surg. Sports. Traumotol. Arthrosc.* Mar. 2010; 18(3): 292-7

Zhang X. Guotai J, Wu C, Woo S. L-Y. A Subject Specific Finite Element Model of the Anterior Cruciate Ligament. *IEEE EMBS Conference Procedings.* August 2008.

.